Revealing the combined roles of Aβ and tau in Alzheimer's disease via a pathophysiological activity decoder

Lazaro M. Sanchez-Rodriguez[1,2,3], Gleb Bezgin[1,2,3,4], Felix Carbonell[5], Joseph Therriault[1,2,4], Jaime Fernandez-Arias[1,2,4], Thomas K. Karikari[6,7], Nicholas J. Ashton[6,8,9,10], Andréa L. Benedet[6], Henrik Zetterberg[6,11,12,13,14,15], Kaj Blennow[6,15], Gallen Triana-Baltzer[16], Hartmuth C. Kolb[16], Pedro Rosa-Neto [1,4], Yasser Iturria-Medina[1,2,3*]

[1]Department of Neurology and Neurosurgery, McGill University, Montreal, Canada.

[2]McConnell Brain Imaging Centre, Montreal Neurological Institute, Montreal, Canada.

[3]Ludmer Centre for Neuroinformatics & Mental Health, Montreal, Canada.

[4]McGill University Research Centre for Studies in Aging, Douglas Research Centre, Montreal, Canada.

[5]Biospective Inc., Montreal, Canada.

[6]Department of Psychiatry and Neurochemistry, Institute of Neuroscience and Physiology, The Sahlgrenska Academy at the University of Gothenburg, Mölndal, Sweden.

[7]Department of Psychiatry, School of Medicine, University of Pittsburgh, Pittsburgh, PA, USA.

[8]King's College London, Institute of Psychiatry, Psychology and Neuroscience Maurice Wohl Institute Clinical Neuroscience Institute London UK.

[9]NIHR Biomedical Research Centre for Mental Health and Biomedical Research Unit for Dementia at South London and Maudsley NHS Foundation London UK.

[10]Centre for Age-Related Medicine, Stavanger University Hospital, Stavanger, Norway.

[11]Department of Neurodegenerative Disease, UCL Institute of Neurology, Queen Square, London, UK.

[12]UK Dementia Research Institute at UCL, London, UK.

[13]Hong Kong Center for Neurodegenerative Diseases, Clear Water Bay, Hong Kong, China.

[14]Wisconsin Alzheimer's Disease Research Center, University of Wisconsin School of Medicine and Public Health, University of Wisconsin-Madison, Madison, WI, USA.

[15]Clinical Neurochemistry Laboratory, Sahlgrenska University Hospital, Mölndal.

[16]Neuroscience Biomarkers, Janssen Research & Development, La Jolla, California, USA.

[*]Corresponding author: YIM (yasser.iturriamedina@mcgill.ca)

Abstract

Neuronal dysfunction and cognitive deterioration in Alzheimer's disease (AD) are likely caused by multiple pathophysiological factors. However, evidence in humans remains scarce, necessitating improved non-invasive techniques and integrative mechanistic models. Here, we develop and validate a personalized brain activity model that incorporates functional MRI, amyloid-β (Aβ) and tau-PET from AD-related participants (N=132). By simulating electrophysiological activity mediated by toxic protein deposition, this integrative approach uncovers key patho-mechanistic interactions, including synergistic Aβ and tau effects on cognitive impairment and neuronal excitability increases with disease progression. The data-derived neuronal excitability values strongly predict clinically relevant AD plasma biomarker concentrations (p-tau217, p-tau231, p-tau181, GFAP). Furthermore, our results reproduce hallmark AD electrophysiological alterations (theta band activity enhancement and alpha reductions) which occur with Aβ-positivity and after limbic tau involvement. Microglial activation influences on neuronal activity are less definitive, potentially due to neuroimaging limitations in mapping neuroprotective vs detrimental phenotypes. Mechanistic brain activity models can further clarify intricate neurodegenerative processes and accelerate preventive/treatment interventions.

Introduction

Neurodegenerative conditions are highly complex, with several pathological factors interacting across multiple spatial and temporal scales[1,2]. Alzheimer's disease (AD) is defined by synaptic and neuronal degeneration and loss accompanied by amyloid beta (Aβ) plaques and tau neurofibrillary tangles (NFTs)[3,4]. Additional factors play critical roles in AD pathogenesis, including vascular, metabolic and neuroinflammatory dysregulations[5–7]. These disease processes also manifest differently given subject-specific genetic and environmental conditions[1,8]. Models of multiple pathological markers and physiology can help reveal the connection between individual AD fingerprints and cognitive deficits[3,9,10].

AD also associates with several neuro-functional alterations which constitute a reliable readout for brain network degeneration[2,3,10–12]. Patients present distinct blood-oxygen-level-dependent (BOLD) signal content in the low frequency fluctuations range (0.01–0.08 Hz)[12,13]. These differences increase with disease progression, from cognitively unimpaired (CU) controls to mild cognitive impairment (MCI) to AD, correlating with performance on cognitive tests[12]. Another characteristic functional change is the slowing of the electro-(magneto-) encephalogram E/MEG, with the signal shifting towards low frequency bands[10,11]. Electrophysiological spectral changes associate with brain atrophy and with losing connections to hub regions including the hippocampus, occipital and posterior areas of the default mode network[14]. All these damages are known to occur in parallel with cognitive impairment[14]. However, the underlying pathophysiological mechanisms remain under scientific debate[3].

Mounting evidence across spatiotemporal scales and experimental setups suggest that neuronal excitability changes are a key mechanistic event appearing early in AD and a tentative

therapeutic target to reverse disease symptoms[3,15–17]. Cortical and hippocampal network hyperexcitability precedes memory impairment in AD models[15,18]. *In-vivo* animal experiments indicate that both Aβ and tau pathologies synergistically interact to impair neuronal circuits[16]. For example, the hypersynchronous epileptiform activity observed in over 60% of AD cases[19] may be generated by surrounding Aβ and/or tau deposition increasing network hyperactivity[19,20]. In an apparent feedback loop, endogenous neuronal activity, in turn, regulates Aβ aggregation, in both animal models and computational simulations[21,22]. Microglial activation can also influence neuronal firing and act on hypo/hyperexcitation patterns while leading to inflammatory responses[6,7]. However, due to experimental limitations, it remains unclear how these multiple pathological factors interact to directly alter neuronal activity in AD's neurodegenerative progression.

Large-scale neuronal dynamical models represent a promising avenue for clarifying pathophysiological mechanisms[23,24]. Generative modeling of brain re-organization has been used to test disease-specific hypotheses by focusing on the corresponding causal mechanisms[25–27]. By considering brain topology (the structural connectome[10]) and regional profiles of a pathological agent[26], it is possible to recreate how a disorder develops, providing supportive or conflicting evidence on the validity of a hypothesis[25]. Models follow average activity in relatively large groups of excitatory and inhibitory neurons (neural masses), with large-scale interactions generating E/MEG signals and/or functional MRI observations[28]. Through neural mass modeling, personalized virtual brains were built to describe Aβ pathology effects on AD-related EEG slowing[27]. Simulated resting-state functional MRI across the AD spectrum was used to estimate biophysical parameters associated with cognitive deterioration[29]. In addition, different intervention strategies to counter neuronal hyperactivity in AD have been tested[9,22], illustrating

another key advantage of mechanistic causal modeling: the design of personalized treatments[1,3,8,10,25,26]. Notably, computational approaches also offer accurate tools to quantify biological parameters that are not measurable with non-invasive techniques[30], like neuronal excitability values, which would allow us to characterize sources of functional hyperactivity[28].

Here, we considerably extend previous mechanistic brain models of disease progression in four fundamental ways. First, we develop a personalized whole-brain neural mass model integrating multilevel, multifactorial pathophysiological profiles to clarify their causal impact on neuronal activity alterations. Second, using *in-vivo* functional MRI together with Aβ- and tau-positron emission tomography (PET), we quantify the combined impact of these relevant AD pathophysiological factors on neuronal excitability. Third, we investigate the subsequent associations between pathophysiological neuronal activity affectations and clinically applicable blood-plasma biomarkers (p-tau217, p-tau231, p-tau181, GFAP) as well as cognitive integrity. Fourth, we reproduce hallmark AD electrophysiological alterations and pinpoint their associated critical toxic protein accumulation stages. Overall, our results expand previous understandings of neuropathological impact on AD, namely the emergence of neuronal hyperactivity[3,15–17], slowing of the E/MEG signals[10,11] and the existence of synergistic multifactorial interactions[1,16]. These findings support the premise of using integrative neural mass models to decode multilevel mechanisms in complex neurological disorders.

Results

Modeling pathophysiological impacts on whole-brain neuronal activity

A personalized generative framework to study the combined pathophysiological effect of Aβ and tau on neuronal activity was formulated in terms of a whole-brain neuronal mass model (see Fig. 1). This model assumes that, at each brain region, neuronal excitability is potentially mediated by the local pathophysiological burden, specifically by PET-measured accumulation of Aβ plaques, tau tangles and the combined Aβ and tau deposition (their synergistic interaction). In addition, the neuronal populations interact via nervous fibers, potentially propagating pathophysiological effects across each individual brain's anatomical connectome [1,31]. Altogether, this framework serves to generate continuous pathophysiologically-mediated neuronal activities, which are transformed into BOLD signals by a hemodynamic-metabolic module (*Methods*, *Integrative neuronal activity simulator*). The individual model parameters quantifying the brain-wide influence of each neuropathological factor (or their synergistic interaction) on neuronal excitability are identified by maximizing the similarity between the generated and observed BOLD data. These estimated parameters serve to reconstruct hidden electrophysiological signals, neuronal excitability spatial profiles, and to study additive relationships with plasma biomarkers and cognitive integrity.

Data from one hundred thirty-two individuals from the Translational Biomarkers in Aging and Dementia cohort (TRIAD, https://triad.tnl-mcgill.com/) were used in the study, including CU (N=81), MCI (N=35) and AD (N=16) participants (Supplementary Table 1). All subjects were cognitively profiled (e.g., MMSE[32], MoCA[33]) and underwent structural and resting-state functional MRI and Aβ (^{18}F-NAV4694)-, tau (^{18}F-MK-6240)- and microglial activation (^{11}C-PBR28)-PET. From the fMRI signals, regional fractional amplitudes of low-frequency fluctuations (fALFF) values were obtained, a measure consistently identified as a reliable neuronal activity biomarker of AD's progression[12,13]. From all the PET images, the

corresponding mean Standardized Uptake Value Ratios (SUVRs)[1,34,35] were extracted for 66 bilateral regions of interest defined according to the Desikan-Killiany-Tourville (DKT) atlas[36], using the cerebellar grey matter as the reference region (*Methods*, *Image processing*). Individuals also had measures of plasma p-tau[37–40] and glial fibrillary acidic protein[41] (*Methods*, *Plasma biomarkers*).

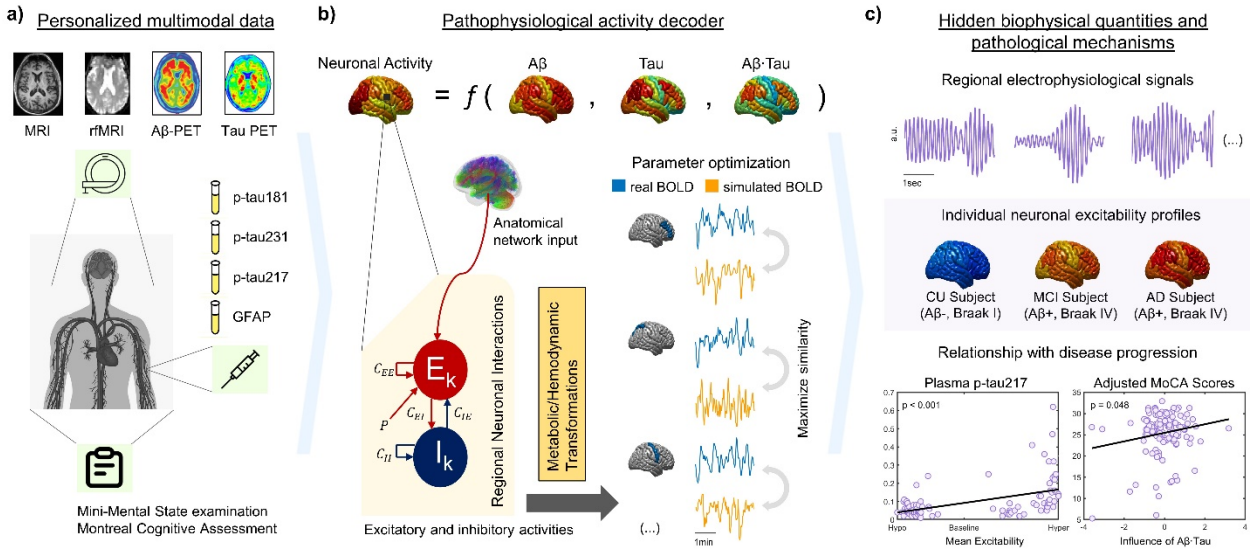

Fig. 1: Schematic Pathophysiological Activity Decoder. a) Individuals underwent a multimodal assessment including structural and resting-state functional MRI, Aβ and tau-PET, clinically relevant plasma biomarkers, and cognitive evaluations. **b**) In the Alzheimer's disease model, neuronal excitability is defined as a function of Aβ, tau and the synergistic interaction of Aβ and tau. Regional excitatory and inhibitory firing rates are influenced by the local pathophysiological profiles and the signals coming from other regions via the anatomical connectome. The regional neuronal signals generate BOLD indicators through metabolic/hemodynamic transformations. By maximizing the similarity between the generated and observed BOLD data, the set of subject-specific influences of pathophysiological factors on neuronal activity are quantified. **d**) These estimated pathophysiological influences serve to

recover electrophysiological activity producing the real individual BOLD signals, and to study individual excitability profiles and their relationship with independent AD (plasma) markers and cognitive deterioration.

Reproducing hallmark electrophysiological alterations in AD progression

A desired attribute of biologically-defined generative tools in clinical applications is to reproduce and mechanistically clarify reported pathophysiological observations. We obtained subject-specific relative contributions of the considered pathophysiological factors on neuronal activity and reconstructed proxy quantities for electro-(magneto-)encephalographic (E/MEG) sources in each brain region. Subsequently, we aimed to test the proposed pathophysiological - activity generator's ability to validate reported spectral changes in AD, i.e., increases of theta band power (4–8 Hz) and decreases of power in the lower alpha band (alpha1, 8–10 Hz)[9–11]. Among the quantities contributing to the E/MEG model output, we also closely studied excitatory firings and changes to their magnitude given the influence of the toxic protein depositions (for definitions and further details on the calculations, see *Methods, Integrative neuronal activity simulator*). The participants were separated into groups according to their clinical diagnosis (CU, MCI, AD) and Aβ-positivity or Braak stages (see *Methods, Imaging Processing, PET*).

We observed that the standardized ratio of power in the theta band (4–8 Hz) was higher for Aβ+ groups than for Aβ- (Fig. 2a) – see also *Methods, Statistical analyses* and Supplementary Table 2. Conversely, the alpha1 (8–10 Hz) power decreased with Aβ-positivity. Finally, the average excitatory firings were generally higher for Aβ+ subjects. Similar results

were observed across Braak stages (Fig. 2b). Interestingly, Braak II was the turning point for a change in the sign of the standardized quantities (as compared to CU(Aβ+) in Fig. 2a) indicating higher theta power and excitatory activity and lower alpha1 power after this stage. Braak III participants, a group with small sample size, did not clearly present the behavior shown by other groups from Braak II and on. In addition, significant differences between mean excitatory activities in Braak II and Braak VI subjects appeared.

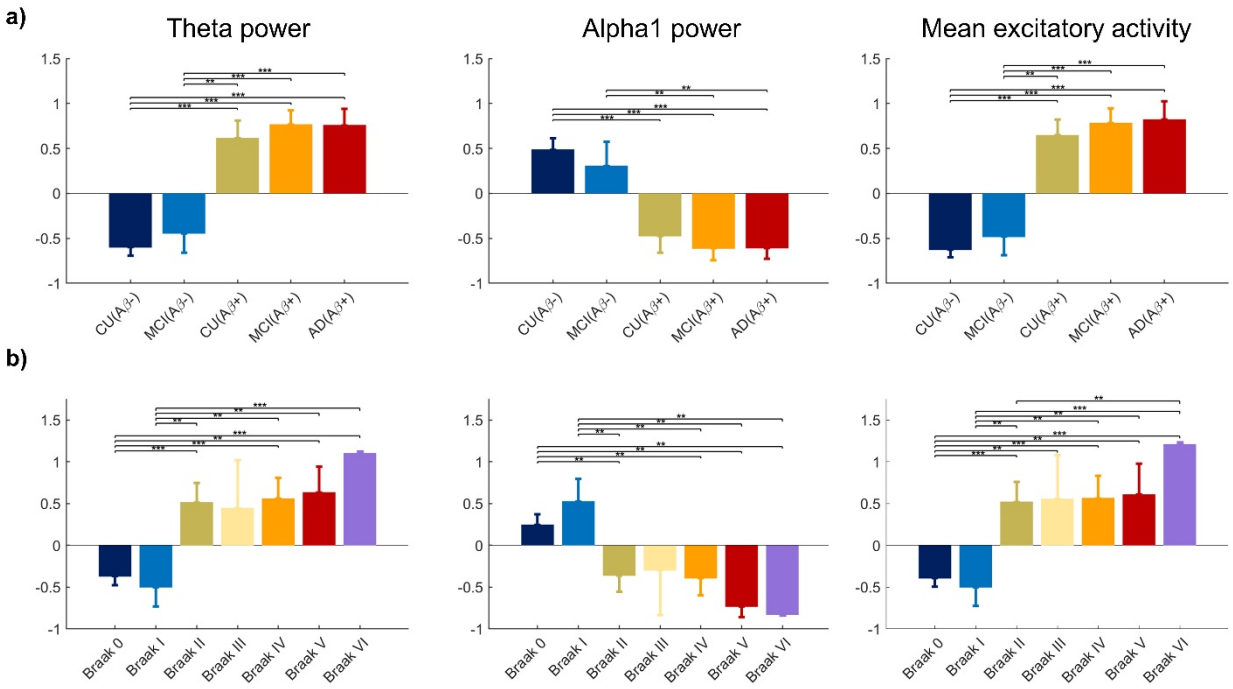

Fig. 2: Electrophysiological impacts by *Aβ, tau, Aβ·tau*. From left to right: ratio of power in the theta band (4–8 Hz) of the regional excitatory input currents (the E/MEG is proportional to the excitatory input current), ratio of power in the alpha1 band (8–10 Hz) and mean excitatory firings (over all regions and time points). Each of the quantities was standardized using the mean and s.d. from all subjects, for visualizing general trends. The bars represent group averages and standard errors. The results of ANCOVA post-hoc t-tests for the above-mentioned groups, with the corresponding electrophysiological quantity as response variable and age and sex as

covariates are also shown. ** represents significance level $p < 0.01$ and *** means significance level $p < 0.001$. Participants were grouped according to clinical diagnosis and Aβ-positivity (**a**) and Braak stages (**b**).

Differences in neuronal excitability explain clinical states and disease progression

Seeking to find mechanisms underlying the observed electrophysiological patterns, we reconstructed the biophysical quantity that changes due to the influence of the pathological factors in our model: neuronal excitability. Fig. 3 and Supplementary Fig. 1 show excitability values for all brain regions of interest and subjects. The combined action of the pathological factors either increases ("hyper") or decreases ("hypo") regional excitability around a certain baseline normal value.

We found significant differences of neuronal excitability due to Aβ positivity and Braak stages. Firstly, we observed significant discrimination between all Aβ - and Aβ+ groups (Fig. 3), i.e.: CU(Aβ-) and CU(Aβ +), MCI(Aβ+), AD(Aβ +) ($p < 0.001$, sex and age adjusted); MCI(Aβ-) and CU(Aβ+), MCI(Aβ+), AD(Aβ+) ($p < 0.05$, sex and age adjusted). Additionally, we discovered similar differences between Braak 0 (non-significant neurofibrillary tangle involvement) participants and those in all later stages, and for Braak I and Braak II, IV-VI, and Braak II and Braak VI (Supplementary Fig. 1). Subjects in advanced disease stages generally presented hyperexcitability profiles, while Aβ- and Braak 0-I participants were largely characterized by a slight hypoexcitability.

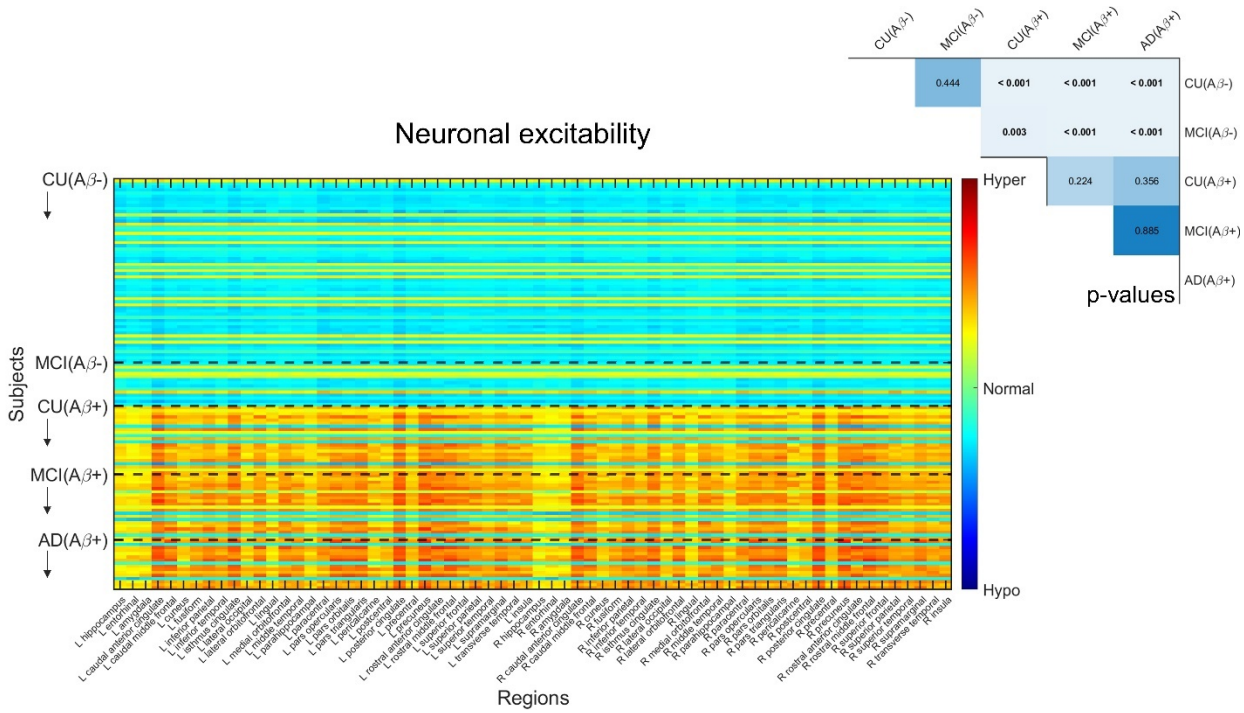

Fig. 3: Neuronal excitabilities under the influence of *Aβ, tau and Aβ·tau*. Inferred neuronal excitability values for the brain regions of interest ("y"-axis) and all subjects ("x"-axis). Participants were grouped according to clinical diagnosis and Aβ-positivity. Within a group, subjects appear according to their existing ordering in the anonymized database. Warm colors represent hyperexcitability of the region in the subject's brain and cool colors denote hypoexcitable states. Results of ANCOVA post-hoc t-tests for the above-mentioned groups, with the average intra-brain excitability values as response variable and age and sex as covariates appear in the upper right. P-values in bold fonts represent differences at a 5% significance level or lower.

Neuronal hyperexcitability relates to high levels of plasma AD biomarkers

In this section, we investigated the relationship between the obtained excitability values and blood biomarkers of AD pathophysiology, which constitute accessible alternatives to

neuroimaging indicators[37,41–43]. Fig. 4 shows the relationships between the obtained average intra-brain excitabilities and the plasma biomarkers p-tau181, p-tau231 and p-tau217 (phosphorylated tau indicators) and glial fibrillary acidic protein (GFAP, a measure of reactive astrogliosis and neuronal damage[41]). Notably, we observed that high levels of the plasma biomarkers significantly relate with the participants' neuronal hyperactivation.

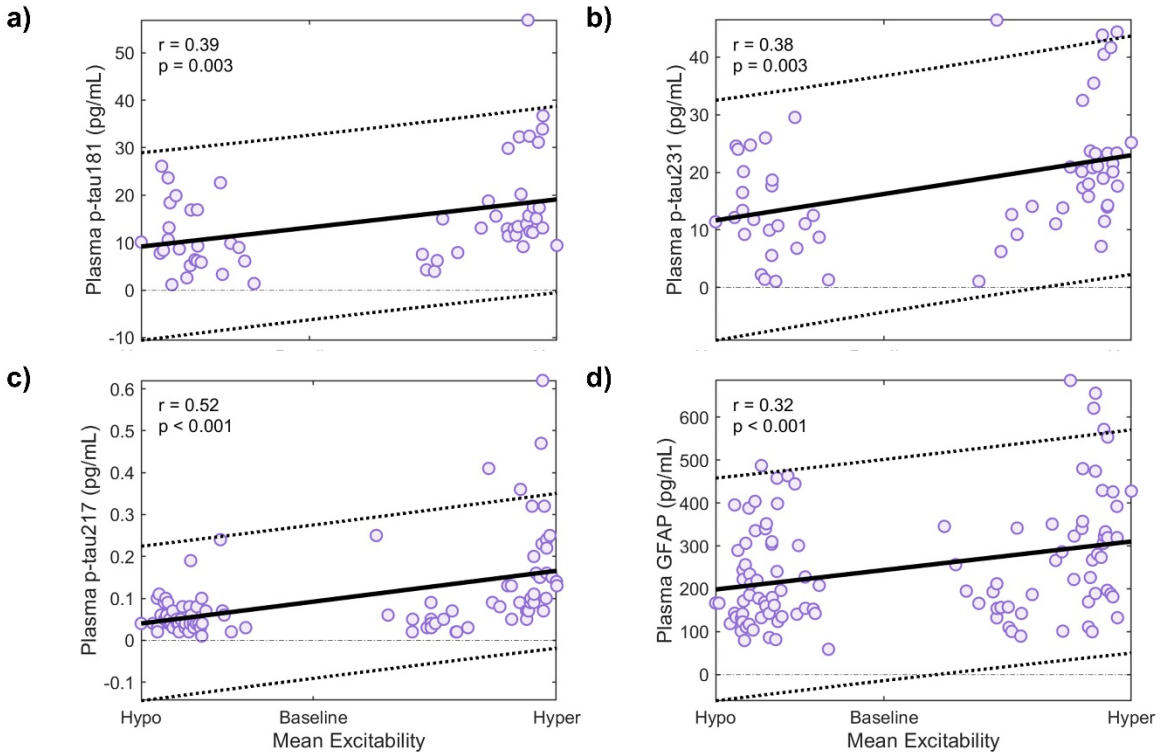

Fig. 4: Neuronal excitabilities and AD plasma biomarkers. Spearman's correlation analyses between plasma biomarkers and estimated average intra-brain excitabilities, for **a**) p-tau181, **b**) p-tau231, **c**) p-tau217 and **c**) GFAP. The error bands denote 95% confidence intervals (CIs).

Synergistic Aβ and tau interaction strongly relates to cognitive performance

Finally, we proceeded to estimate the pathophysiological factors' effects on cognitive impairment through the changes in neuronal activity, measured with the individual weights contributing to neuronal excitability. Table 1 shows the results of regression analyses taking MMSE and MoCA scores as response variables, and the obtained model influences of Aβ, tau and the Aβ·tau interaction as predictors, while adjusting by sex, age and education (*Methods, Statistical analyses*). We observed that both the Aβ's solo influence on neuronal activity and the Aβ·tau synergistic interaction term were significant predictors of MMSE and MoCA evaluations ($p < 0.05$). The coefficients of these terms in the linear models were positive in all cases. Thus, highly negative influences of the studied pathophysiological factors – yielding hyperexcitability in the model (*Methods, Integrative neuronal activity simulator)*– invariably associated with low cognitive scores.

Table 1. Multiple linear regression analysis investigating the pathological effects on neuronal activity as predictors of MMSE and MoCA scores

MMSE scores			
	β	95% CI of β	p
Intercept	22.463	[15.591 29.335]	< 0.001
$\theta^{A\beta}$	**0.791**	**[0.092 1.489]**	**0.027**
θ^{Tau}	0.138	[-0.581 0.857]	0.705
$\theta^{A\beta \cdot Tau}$	**1.040**	**[0.371 1.710]**	**0.002**
Sex	-1.505	[-2.872 -0.139]	0.031
Age	0.064	[-0.025 0.152]	0.156
Education	0.095	[-0.096 0.286]	0.326
MoCA scores			
	β	95% CI of β	p
Intercept	18.702	[8.656 28.748]	< 0.001
$\theta^{A\beta}$	**1.598**	**[0.618 2.579]**	**0.002**
θ^{Tau}	-0.020	[-0.973 0.932]	0.967
$\theta^{A\beta \cdot Tau}$	**1.006**	**[0.009 2.004]**	**0.048**
Sex	-2.379	[-4.298 -0.460]	0.015

Age	0.096	[-0.034 0.226]	0.148
Education	0.046	[-0.222 0.314]	0.735

The influences of Aβ plaques ($\theta_E^{A\beta}$), tau tangles (θ_E^{Tau}) and the interaction of Aβ and tau ($\theta_E^{A\beta \cdot Tau}$) on neuronal activity, sex and age were considered as predictors. Reported values are obtained coefficients (β), the 95% confidence intervals and the p-values for the t-statistic of the two-sided hypothesis tests. Significant terms (5% level) other than the intercepts are highlighted. MMSE: R^2=0.18, $p < 0.001$; MoCA: R^2=0.19, $p < 0.001$. MMSE, Mini-Mental State examination; MoCA, Montreal Cognitive Assessment.

Discussion

We developed an integrative biophysical framework to map pathophysiological influences on neuronal activity, with application to AD. Previous work has investigated how pathological electrophysiological activity emerges in generative models that consider the influence of isolated biological factors, such as Aβ plaques[27] or in several possible AD synaptic dysfunction scenarios[9,22]. Additionally, multifactorial dynamic interactions propagating through anatomical and vascular networks were individually characterized in the AD spectrum[1,2,44,45]. Building on the strengths of such studies, our approach decodes, for the first time, the subject-specific simultaneous and combined pathological neuronal activity contributions of relevant disease factors: Aβ and tau, evaluated through individual functional MRI and PET biomarkers. Altogether, we observed increased neuronal excitability with AD progression, which also predicted increased plasma biomarkers concentrations and cognitive impairment.

Our findings confirm previous observations[3,11,15,16,19,20] and cast new light on microscopical pathological processes that are inaccessible to traditional neuroimaging methods. Through considering the influence of multiple pathophysiological factors, we have retrieved the AD electrophysiological hallmark (enhancement of theta band activity together with alpha decreases, as disease progresses[10,11]) from BOLD signals. Our results also indicate that CU(Aβ+) and/or Braak II are the stages from which these electrophysiological biomarkers become abnormal. These groups contain subjects who are not cognitively impaired but present significant Aβ deposition[34] and/or have developed entorhinal and hippocampus tau involvement detectable by tau PET[46]. Our observation suggests that such individuals may be the most likely candidates to benefit from early disease interventions to modify cognitive impairment associated with patho-electrophysiological activity[10,11,14].

No previous direct *in-vivo* evidence for neuronal hyperactivity existed thus far in humans, although proxy measurements[47], post-mortem studies[17] and animal models[16] have suggested a similar mechanism. In this study, by assuming a toxic protein influence model (*Aβ, tau, Aβ·tau*) we inferred neuronal excitability values from the individual PET-functional MRI datasets. The progression towards hyperexcitation with disease worsening was equally evident for a simplified model with separate contributions by Aβ and tau only (Supplementary Figs. 2-3). Increased excitability was also associated with high levels of plasma biomarkers (blood phosphorylated tau and GFAP) which are sensitive to incipient AD pathology[41–43,48,49] and disease progression, especially p-tau217[37,42], further demonstrating the strong biomarker capabilities of our estimated excitability parameters. Additionally, we observed that the more hyperactive the neuronal populations of a subject were (given by negative influence values of the significant factors in our

model), the greater the participant's cognitive dysfunction, thus supporting a direct link among neuronal excitability, pathophysiological burden, and cognitive integrity.

Beyond AD-related protein deposition, our method can also investigate the influence of other critical factors. It has been hypothesized, and to some extent observed[6,7,15], that microglial activation (a probable marker for neuroinflammation[35,50]) affects excitability and neuronal activity in AD. Consequently, we performed a set of complimentary experiments where we recreated the obtained results in a model that also considers deviations to neuronal excitability due to microglial activation –measured with 18kDa Translocator Protein PET. However, we did not find separation between clinical groups in terms of the estimated neuronal excitabilities when the microglial activation factor was considered, except Braak 0 vs Braak VI (Supplementary Figs. 4-5). Moreover, the synergistic interaction of Aβ and tau was the factor that better predicted cognitive impairment, with no significant effect by the microglial activation term (Supplementary Table 3). We attribute this effect to technical limitations associated with the acquisition of microglial activation. Unlike the Aβ and tau PET SUVRs data, which showed extended statistically significant differences across all brain regions for CU and AD participants (two-sampled t-test, $p < 0.05$), microglial activation images exhibited differences in only 24 regions (i.e., approx. 36%; Supplementary Table 4). Microglial activation is thought to have a neuroprotective character (M2-phenotype) at early disease stages[6,7]. On the other hand, excessive activation of microglia seemingly becomes detrimental in clinical AD (M1-phenotype) by releasing pro-inflammatory cytokines that may exacerbate AD progression[6,7,35]. Nevertheless, modern neuroinflammation PET tracers are not specific to these two different phenotypes as no consistent targets have been discovered[7]. Thus, our extended results albeit being relatively

uninformative in terms of AD-affectations to neuronal excitability, capture intrinsic microglial activation PET mapping insufficiencies. [44]

Our methodology also has several limitations. Although we used state-of-the-art fMRI experiments in this study (TR = 681ms, spatial resolution = 2.5×2.5×2.5 mm^3), more detailed spatiotemporal dynamics could be captured with novel ultra high-resolution functional imaging techniques[51]. On the other hand, by using average anatomical connectivity, we have singled-out the mechanisms by which toxic protein deposition and neuroinflammation are associated with pathological neuronal activity. Personalized therapeutic interventions[1] would require precise individual profiles for increased efficiency. In such applications, including the connectomes' individual variability may be beneficial. Regarding the neuro-physical model for the influence of the pathophysiological factors, two aspects should be considered in future work. Firstly, extending the intra-regional neuronal interactions with additional excitatory and inhibitory populations, pursuing a finer descriptive scale, will also enable us to account for additional significant disease factors such as neuronal atrophy[5]. Secondly, the effects on inhibitory firings should be explored separately as well. Pyramidal (excitatory) neurons greatly outnumber any other neuronal population, making them the most likely proteinopathies target[3]. However, inhibitory populations are key in maintaining healthy firing balances[3] and interacting with glial cells[52].

Our approach has major implications to disease hypothesis testing. Generative models[25] in works by Iturria-Medina et al.[1,2], Deco et al.[26,53], Sotero et al.[10,54], de Haan et al.[9,22] among others, focus on better comprehending neurological conditions. The models considered in the present study reflect plausible biophysical mechanisms determining neuronal activity abnormalities in the AD spectrum[3,6,15,16]. Critical mechanistic information on the underlying

activity-generating processes is obtained, as well as about their relationship with clinical and cognitive profiles. Importantly, we observed that the synergistic interaction of Aβ and tau, and Aβ separate contributions are the most significant factors influencing aberrant neuronal activity, AD progression and symptomatology. In effect, a critical methodological contribution is the capacity to resolve complex biological processes hidden to current non-invasive imaging and electrophysiological monitoring techniques, e.g., the neural masses' firing excitabilities. For future work, we aim to further clarify the specific molecular features responsible for the differences in excitability values across clinical stages. By doing so, we expect to gain further insights into pathophysiology that could boost diagnostic accuracy and preclinical applications. This *pathophysiological activity decoder* is equally applicable to other intricate multifactorial neurological disorders and may well help advance their characterization and efficient treatment at a personalized level.

Methods

Participants

We selected individuals from the Translational Biomarkers in Aging and Dementia (TRIAD) cohort (https://triad.tnl-mcgill.com/). The study was approved by the Douglas Mental Institute Research Board and all participants gave written consent. All subjects underwent MRI, resting-state fMRI, Aβ (^{18}F-NAV4694)-, tau (^{18}F-MK-6240)- and neuroinflammation (^{11}C-PBR28)- PET scans, together with a complete cognitive evaluation, including the Mini-Mental State Examination (MMSE) and the Montreal Cognitive Assessment (MoCA). We chose baseline assessments in all cases. Only participants with "cognitively unimpaired" (N=81), "mild

cognitive impairment" (N=35), or "probable Alzheimer's disease" (N=16) clinical and pathophysiological diagnoses were considered[55].

Image processing

MRI: Brain structural T1-weighted 3D images were acquired for all subjects on a 3 T Siemens Magnetom scanner using a standard head coil. The images were processed following a standard pipeline[1] and mapped to the Desikian-Killiany-Touriner (DKT)[36] atlas for gray matter segmentation. We selected 66 (bilateral) cortical regions (Supplementary Table 4). Subcortical regions, e.g., in the basal ganglia, were not considered given their tendency to present PET off-target binding[56,57].

fMRI: The resting-state fMRI acquisition parameters were: Siemens Magnetom Prisma, echo planar imaging, 860 time points, TR = 681 ms, TE = 32.0 ms, flip angle = 50 deg, number of slices = 54, slice thickness = 2.5 mm, spatial resolution = 2.5×2.5×2.5 mm^3, EPI factor = 88. We applied a minimal processing pipeline[1] including motion correction and spatial normalization to the MNI space[58] using the registration parameters obtained for the structural T1 image. The linear trend was removed as well. We calculated the fractional amplitude of low-frequency fluctuations (fALFF)[12], a regional proxy indicator for neuronal activity that has shown high sensibility to disease progression. Briefly, we transformed the signals for each voxel to the frequency domain and computed the ratio of the power in the low-frequency range (0.01–0.08 Hz) to that of the entire BOLD frequency range (0–0.25 Hz). The fALFF values were ultimately averaged over the voxels according to their belonging to brain regions.

Diffusion Weighted MRI (DW-MRI): High angular resolution diffusion imaging (HARDI) data was acquired for N = 128 in the Alzheimer's Disease Neuroimaging Initiative (ADNI)

(adni.loni.usc.edu). The authors obtained approval from the ADNI Data Sharing and Publications Committee for data use and publication, see documents http://adni.loni.usc.edu/wp-content/uploads/how_to_apply/ADNI_Data_Use_Agreement.pdf and http://adni.loni.usc.edu/wp-content/uploads/how_to_apply/ADNI_Manuscript_Citations.pdf, respectively. More details can be found in a previous publication where ADNI's DW-MRI was processed and analyzed[1]. In a nutshell, region-to-region anatomical connection density matrices were obtained using a fully automated fiber tractography algorithm[59] and intravoxel fiber distribution reconstruction[60]. For any subject and pair of regions k and l , the C_{lk} measure ($0 \leq C_{lk} \leq 1, C_{lk} = C_{kl}$) reflects the fraction of the region's surface involved in the axonal connection with respect to the total surface of both regions. We averaged the ADNI subject-specific connectivity matrices[1,61] to utilize a single, representative anatomical network across our calculations on the TRIAD dataset.

PET: Study participants had Aβ (^{18}F-NAV4694), tau (^{18}F-MK-6240) and translocator protein microglial activation (^{11}C-PBR28) PET imaging in a Siemens high-resolution research tomograph. A bolus injection of ^{18}F-NAV4694 was administered to each participant and brain PET imaging scans were acquired approximately 40-70 min post-injection. The images were reconstructed using an ordered subset expectation maximization (OSEM) algorithm on a 4D volume with three frames (3 × 600 s)[34]. ^{18}F-MK-6240 PET scans of 20 min (4 × 300 s) were acquired at 90-110 min after the intravenous bolus injection of the radiotracer[62]. ^{11}C-PBR28 images were acquired at 60–90 min after tracer injection and reconstructed using the OSEM algorithm on a 4D volume with 6 frames (6 × 300 s)[35]. Images were corrected for attenuation, motion, decay, dead time and random and scattered coincidences. Using the registration parameters obtained for the participants' structural T1 images, all PET images were spatially

normalized to the MNI space. ^{18}F-MK-6240 images were meninges-striped in native space before performing any transformations to minimize the influence of meningeal spillover. SUVR values for the DKT grey matter regions were calculated using the cerebellar gray matter as the reference region.

PET-imaging Aβ status was determined visually by consensus of two neurologists blinded to the diagnosis. The DKT atlas was separately used to define the ROIs for tau-PET Braak stage-segmentation[46,63] which consisted of: Braak I (pathology confined to the transentorhinal region of the brain), Braak II (entorhinal and hippocampus), Braak III (amygdala, parahippocampal gyrus, fusiform gyrus and lingual gyrus), Braak IV (insula, inferior temporal, lateral temporal, posterior cingulate and inferior parietal), Braak V (orbitofrontal, superior temporal, inferior frontal, cuneus, anterior cingulate, supramarginal gyrus, lateral occipital, precuneus, superior parietal, superior frontal and rostromedial frontal) and Braak VI (paracentral, postcentral, precentral and pericalcarine)[46].

Plasma biomarkers

Blood biomarkers were quantified with Single molecule array (Simoa) assays (Quanterix, Billerica, MA). These measurements included tau phosphorylated at threonine 181 (p-tau181)[43], tau phosphorylated at threonine 231 (p-tau231)[42], tau phosphorylated at threonine 217 (p-tau217)[37,40] and glial fibrillary acidic protein (GFAP)[41]and have been previously reported.

Integrative neuronal activity simulator

Electrophysiological model: The electrophysiological brain activity is realized through coupled Wilson-Cowan (WC) modules[64–68]. In this simple formulation, the variables of interest are the firing rates of the excitatory and inhibitory neural masses, $E(t)$ and $I(t)$, respectively. Neural

masses are average neuronal populations describing the dynamic behavior of similar neurons within a given spatial domain, i.e., brain regions[10,64,69]. In WC, the excitatory and inhibitory populations are locally coupled. Moreover, the excitatory population is further stimulated by other local inputs (P) and cortico-cortical connections, C (*Image processing, Diffusion Weighted MRI*). In effect, each l region influences the dynamics of the k region by the quantity $\frac{\eta}{N}\mathsf{C}_{lk}E_l$, where η is a global scaling coupling strength and N is the total number of regions ($N = 66$). We performed a dynamical system analysis[64,65,68,70] and obtained common P and η values simulating plausible electrophysiological oscillations and BOLD signals (Supplementary Fig. 6a) for all participants. The parameters used in this study are reported in Supplementary Table 5.

All the inputs (both local and external) received by a neuron are integrated in time when their sum surpasses a certain threshold, (θ_E or θ_I)[65]. In the neural mass framework, this integration is achieved by means of a sigmoidal activation function[64], $S(x) = \frac{1}{1+\exp[-a(x-\theta)]} - \frac{1}{1+\exp[a\theta]}$ Compared to the "baseline" firings obtained by using the canonical values reported in the literature, regional excitability can be higher (hyperexcitability) or lower (hypoexcitability) depending on whether the firing rate function is shifted to lower or higher input current values, respectively (Supplementary Fig. 6b). In our approach, the regional activity profiles are determined by the excitatory firing, a simplification based on the much larger excitatory prevalence in the cortex[3,17]. We suppose that the regional excitatory firing thresholds are mediated by the following disease factors: Aβ plaques (with a subject-specific contribution weight given by $\theta_E^{A\beta}$), tau tangles (θ_E^{Tau}) and the interaction of amyloid and tau ($\theta_E^{A\beta \cdot Tau}$). These effects are simplistically written as linear fluctuations from the normal baseline value due to the regions' accumulation of each factor (Supplementary Fig. 6c), with the SUVRs normalized to the

[0,1] interval (Supplementary Fig. 7), to preserve the dynamical properties of the desired solution:

$$\theta_{E,k} = \theta_0 + \theta_E^{A\beta} \cdot A\beta_k + \theta_E^{Tau} \cdot Tau_k + \theta_E^{A\beta \cdot Tau} \cdot A\beta_k \cdot Tau_k \qquad (1)$$

A negative contribution by a factor ($\theta_E^{A\beta}$, θ_E^{Tau} or $\theta_E^{A\beta \cdot Tau}$) means that the pathological accumulation of such a biomarker tends to decrease the firing threshold thus yielding hyperexcitability. Given the inverse relationship existing between firing thresholds and effective firing rates, we define regional excitability as $1/\theta_{E,k}$.

The evolution of the average firing rates $E(t)$ and $I(t)$ is then given by the following set of differential equations[64,65,68]:

$$\dot{E}_k = \frac{1}{\tau_E}\left[-E_k + S\left(x_{E,k}\right)\right] \qquad (2)$$

$$\dot{I}_k = \frac{1}{\tau_I}\left[-I_k + S\left(x_{I,k}\right)\right]$$

$$x_{E,k} = C_{EE}E_k - C_{IE}I_k + P + \frac{\eta}{N}\sum_{l=1, l\neq k}^{N} \mathrm{C}_{lk}E_l$$

$$x_{I,k} = C_{EI}E_k - C_{II}I_k$$

Here, the terms $x_{E,k}$ and $x_{I,k}$ are known as the input currents. A synthetic EEG signal is proportional to the regional excitatory input current[67]. Since the BOLD signal is related to the afferent neuronal input[71], we utilized the total action potential arriving to the neuronal populations from other local and external populations as the proxy electrophysiological quantities of interest feeding the metabolic/hemodynamic model by Sotero et al.[54,72].

Metabolic/hemodynamic model: This biophysical model reflects the role that excitatory and inhibitory activities play in generating the BOLD signal[54,72–74]. All variables are normalized to baseline values. Changes in glucose consumption ($g_{E,k}$ and $g_{I,k}$) are linked to the excitatory and inhibitory ($\xi_{E,k}$ and $\xi_{I,k}$) neuronal inputs in region k:

$$\dot{g}_{E,k} = z_{E,k}$$

$$\dot{z}_{E,k} = \frac{-2}{\varkappa_E} z_{E,k} - \frac{1}{\varkappa_E{}^2}\left(g_{E,k} - 1\right) + \frac{h_E}{\varkappa_E}\left(\xi_{E,k} - 1\right)$$

$$\dot{g}_{I,k} = z_{I,k}$$

$$\dot{z}_{I,k} = \frac{-2}{\varkappa_I} z_{I,k} - \frac{1}{\varkappa_I{}^2}\left(g_{I,k} - 1\right) + \frac{h_I}{\varkappa_I}\left(\xi_{I,k} - 1\right)$$

The metabolic rates of oxygen for excitatory ($m_{E,k}$) and inhibitory ($m_{I,k}$) activities, and the total oxygen consumption, m_k, are obtained from the glucose variables.

$$m_{E,k}(t) = \frac{2 - x(t)}{2 - x_0} g_{E,k}(t)$$

$$m_{I,k}(t) = g_{I,k}(t)$$

$$m_k(t) = \frac{\gamma m_{E,k}(t) + m_{I,k}(t)}{\gamma + 1}$$

$$x(t) = \frac{1}{1 + exp\left[c\left(d - g_{E,k}(t)\right)\right]}$$

Next, CBF dynamics (f_k) is modeled as follows[75], assuming that CBF is coupled to excitatory activity:

$$\dot{f}_k = y_k$$

$$\dot{y}_k = \frac{-2}{\varkappa_f} y_k - \frac{1}{{\varkappa_f}^2}(f_k - 1) + \mu(\xi_{E,k} - 1)$$

The outputs of the metabolic and vascular models are converted to normalized cerebral blood volume (b_k) and deoxy-hemoglobin (q_k) content through the Balloon model[76]:

$$\dot{b}_k = \frac{1}{\varkappa_0}(f_k - f_{out})$$

$$\dot{q}_k = \frac{1}{\varkappa_0}\left(m_k - f_{out}\frac{q_k}{b_k}\right)$$

$$f_{out} = {b_k}^{\frac{1}{\zeta}}$$

The BOLD signal is obtained by using a linear observation equation as in:

$$BOLD_k(t) = V_0\big(a_1(1 - q_k) - a_2(1 - b_k)\big)$$

where $a_1 = 4.3\Upsilon_0 E_0 \cdot TE + \varepsilon r_0 E_0 \cdot TE$ and $a_2 = \varepsilon r_0 E_0 \cdot TE + \varepsilon - 1$ are parameters that depend on the experimental conditions (field strength, TE)[77–79]. The interpretation and specific parameter values of the metabolic/hemodynamic transformations resulting in the simulated BOLD signal can be found in Supplementary Table 6. The sets of equations above were solved with an explicit Runge-Kutta (4,5) method, ode45, as implemented in MATLAB 2021b (The MathWorks Inc., Natick, MA, USA) and a timestep of 0.001s.

Parameter estimation: From the simulated BOLD signals, we compute regional fALFF values and minimize their similarity (correlation) with real BOLD indicators, for each participant (Supplementary Fig. 6d). The estimation of the optimal pathological influences set ($\theta_E^{A\beta}, \theta_E^{Tau}, \theta_E^{A\beta \cdot Tau}$) was performed via surrogate optimization (MATLAB 2021b's surrogateopt). This parameter optimization method performs few objective function evaluations hence it is

well-suited for expensive functions as it is the case of our high-dimensional BOLD-simulating dynamical system. We constrained the pathological influences on a small interval around the nominal parameter value (Supplementary Table 5)[64–68] to compare results across subjects and disease states. Then, we performed optimization iterations until no new feasible points were found in the allowed interval.

Interpreting the pathophysiological effects on neuronal activity: The obtained pathological influences ($\theta_E^{A\beta}, \theta_E^{Tau}, \theta_E^{A\beta \cdot Tau}$) describe subject-specific interactions determining brain activity. We use these weights to reconstruct otherwise hidden electrophysiological quantities of interest. Individual neuronal excitability patterns[9] are mapped through equation (1) and can be related to separate measurements like plasma biomarkers for AD[41–43]. Grand average excitatory activities are found by averaging the firing rates $E_k(t)$ over the regions and time points[9], for every subject. Likewise, the input currents of equation (2) are used as proxy measures for cortical sources of resting-state EEG[67]. We perform a Fast Fourier Transformation power analysis of the neural masses' signals and determine the relative power of the traditional rhythms, in particular: theta (4–8 Hz) and alpha 1 (8–10 Hz) frequency band oscillations[9]. Additionally, we investigate the relationship of the obtained pathophysiological influences with cognition[32,33].

Statistical analyses

Group-differences in the electrophysiological quantities of interest (average intra-brain theta and alpha1 power, excitatory firing activity and excitability) were evaluated with ANCOVA post-hoc t-tests, i.e., we looked at the effects of the clinical groups and Aβ positivity/Braak stages on the corresponding quantity, accounting for age and sex. The associations between excitability and plasma biomarkers were tested using Spearman's Rho correlation (large-sample approximation). In addition, to assess the relationship between the pathophysiological factors and cognitive

integrity we fitted multiple linear regression models using the following specifications: $MMSE\ score \sim 1 + \theta_E^{A\beta} + \theta_E^{Tau} + \theta_E^{A\beta \cdot Tau} + sex + age + education$ and $MoCA\ score \sim 1 + \theta_E^{A\beta} + \theta_E^{Tau} + \theta_E^{A\beta \cdot Tau} + sex + age + education$. Each of the factors were standardized using the mean and s.d. from all subjects.

Data availability

All the data collected under the TRIAD cohort is governed by the policies set by the Research Ethics Board Office of the McGill University, Montreal and the Douglas Research Center, Verdun. Researchers can access the TRIAD data for research purpose by submitting a data share request via https://triad.tnl-mcgill.com/contact-us/.

Code availability

The code utilized in this article for the neuronal activity simulations and quantification of the pathological effects is freely available at the lab's website (NeuroPM Lab, https://www.neuropm-lab.com/publication-codes.html).

References

1. Iturria-Medina, Y., Carbonell, F. M. & Evans, A. C. Multimodal imaging-based therapeutic fingerprints for optimizing personalized interventions: Application to neurodegeneration. *Neuroimage* **179**, 40–50 (2018).

2. Iturria-Medina, Y., Carbonell, F. M., Sotero, R. C., Chouinard-Decorte, F. & Evans, A. C. Multifactorial causal model of brain (dis)organization and therapeutic intervention: Application to Alzheimer's disease. *Neuroimage* **152**, 60–77 (2017).

3. Maestú, F., de Haan, W., Busche, M. A. & DeFelipe, J. Neuronal Excitation/Inhibition imbalance: a core element of a translational perspective on Alzheimer pathophysiology. *Ageing Res Rev* **69**, 101372 (2021).

4. Jack, C. R. *et al.* NIA-AA Research Framework: Toward a biological definition of Alzheimer's disease. *Alzheimer's and Dementia* vol. 14 535–562 Preprint at https://doi.org/10.1016/j.jalz.2018.02.018 (2018).

5. Iturria-Medina, Y. *et al.* Early role of vascular dysregulation on late-onset Alzheimer's disease based on multifactorial data-driven analysis. *Nat Commun* **7**, 11934 (2016).

6. Kwon, H. S. & Koh, S. H. Neuroinflammation in neurodegenerative disorders: the roles of microglia and astrocytes. *Translational Neurodegeneration* vol. 9 Preprint at https://doi.org/10.1186/s40035-020-00221-2 (2020).

7. Shen, Z., Bao, X. & Wang, R. Clinical PET imaging of microglial activation: Implications for microglial therapeutics in Alzheimer's disease. *Frontiers in Aging Neuroscience* vol. 10 Preprint at https://doi.org/10.3389/fnagi.2018.00314 (2018).

8. Iturria-Medina, Y. *et al.* Integrating molecular, histopathological, neuroimaging and clinical neuroscience data with NeuroPM-box. *Commun Biol* **4**, (2021).

9. van Nifterick, A. M. *et al.* A multiscale brain network model links Alzheimer's disease-mediated neuronal hyperactivity to large-scale oscillatory slowing. *Alzheimers Res Ther* **14**, 101 (2022).

10. Sanchez-Rodriguez, L. M. *et al.* Design of optimal nonlinear network controllers for Alzheimer's disease. *PLoS Comput Biol* **14**, e1006136 (2018).

11. Babiloni, C. *et al.* Cortical Sources of Resting State EEG Rhythms are Sensitive to the Progression of Early Stage Alzheimer's Disease. *Journal of Alzheimer's Disease* **34**, 1015–1035 (2013).

12. Yang, L. *et al.* Gradual Disturbances of the Amplitude of Low-Frequency Fluctuations (ALFF) and Fractional ALFF in Alzheimer Spectrum. *Front Neurosci* **12**, 1–16 (2018).

13. Yang, L. *et al.* Frequency-dependent changes in fractional amplitude of low-frequency oscillations in Alzheimer's disease: a resting-state fMRI study. *Brain Imaging Behav* **14**, 2187–2201 (2020).

14. Maestú, F. *et al.* The Importance of the Validation of M/EEG With Current Biomarkers in Alzheimer's Disease. *Front Hum Neurosci* **13**, 1–10 (2019).

15. Targa Dias Anastacio, H., Matosin, N. & Ooi, L. Neuronal hyperexcitability in Alzheimer's disease: what are the drivers behind this aberrant phenotype? *Translational Psychiatry* vol. 12 Preprint at https://doi.org/10.1038/s41398-022-02024-7 (2022).

16. Busche, M. A. & Hyman, B. T. Synergy between amyloid-β and tau in Alzheimer's disease. *Nat Neurosci* **23**, 1183–1193 (2020).

17. Lauterborn, J. C. *et al.* Increased excitatory to inhibitory synaptic ratio in parietal cortex samples from individuals with Alzheimer's disease. *Nat Commun* **12**, 2603 (2021).

18. Kazim, S. F. *et al.* Early-onset network hyperexcitability in presymptomatic Alzheimer's disease transgenic mice is suppressed by passive immunization with anti-human APP/Aβ antibody and by mGluR5 blockade. *Front Aging Neurosci* **9**, (2017).

19. Vossel, K. A., Tartaglia, M. C., Nygaard, H. B., Zeman, A. Z. & Miller, B. L. Epileptic activity in Alzheimer's disease: causes and clinical relevance. *Lancet Neurol* **16**, 311–322 (2017).

20. Tok, S. *et al.* Pathological and neurophysiological outcomes of seeding human-derived tau pathology in the APP-KI NL-G-F and NL-NL mouse models of Alzheimer's Disease. *Acta Neuropathol Commun* **10**, (2022).

21. Bero, A. W. *et al.* Neuronal activity regulates the regional vulnerability to amyloid-β 2 deposition. *Nat Neurosci* **14**, 750–756 (2011).

22. de Haan, W., van Straaten, E. C. W., Gouw, A. A. & Stam, C. J. Altering neuronal excitability to preserve network connectivity in a computational model of Alzheimer's disease. *PLoS Comput Biol* **13**, (2017).

23. Deco, G. & Kringelbach, M. L. Great expectations: Using whole-brain computational connectomics for understanding neuropsychiatric disorders. *Neuron* vol. 84 892–905 Preprint at https://doi.org/10.1016/j.neuron.2014.08.034 (2014).

24. Breakspear, M. Dynamic models of large-scale brain activity. *Nature Neuroscience* vol. 20 340–352 Preprint at https://doi.org/10.1038/nn.4497 (2017).

25. Luppi, A. I. *et al.* Dynamical models to evaluate structure–function relationships in network neuroscience. *Nature Reviews Neuroscience* Preprint at https://doi.org/10.1038/s41583-022-00646-w (2022).

26. Deco, G. *et al.* Whole-Brain Multimodal Neuroimaging Model Using Serotonin Receptor Maps Explains Non-linear Functional Effects of LSD. *Current Biology* **28**, 3065-3074.e6 (2018).

27. Stefanovski, L. *et al.* Linking Molecular Pathways and Large-Scale Computational Modeling to Assess Candidate Disease Mechanisms and Pharmacodynamics in Alzheimer's Disease. *Front Comput Neurosci* **13**, 1–27 (2019).

28. Iturria-Medina, Y. & Evans, A. C. Networks-Mediated Spreading of Pathology in Neurodegenerative Diseases. in *Brain Network Dysfunction in Neuropsychiatric Illness* 171–186 (Springer International Publishing, 2021). doi:10.1007/978-3-030-59797-9_9.

29. Zimmermann, J. *et al.* Differentiation of Alzheimer's disease based on local and global parameters in personalized Virtual Brain models. *Neuroimage Clin* **19**, 240–251 (2018).

30. Falcon, M. I., Jirsa, V. & Solodkin, A. A new neuroinformatics approach to personalized medicine in neurology: The Virtual Brain. *Current Opinion in Neurology* vol. 29 429–436 Preprint at https://doi.org/10.1097/WCO.0000000000000344 (2016).

31. Iturria-Medina, Y. & Evans, A. C. On the central role of brain connectivity in neurodegenerative disease progression. *Frontiers in Aging Neuroscience* vol. 7 Preprint at https://doi.org/10.3389/fnagi.2015.00090 (2015).

32. Folstein, M. F., Folstein, S. E. & Mchugh, P. R. *'MINI-MENTAL STATE' A PRACTICAL METHOD FOR GRADING THE COGNITIVE STATE OF PATIENTS FOR THE CLINICIAN*. J. gsychiaf. Res* vol. 12 (1975).

33. Nasreddine, Z. S. *et al.* The Montreal Cognitive Assessment, MoCA: A brief screening tool for mild cognitive impairment. *J Am Geriatr Soc* **53**, 695–699 (2005).

34. Therriault, J. *et al.* Determining amyloid-b positivity using 18F-AZD4694 PET imaging. *Journal of Nuclear Medicine* vol. 62 247–252 Preprint at https://doi.org/10.2967/jnumed.120.245209 (2021).

35. Pascoal, T. A. *et al.* Microglial activation and tau propagate jointly across Braak stages. *Nat Med* **27**, 1592–1599 (2021).

36. Klein, A. & Tourville, J. 101 Labeled Brain Images and a Consistent Human Cortical Labeling Protocol. *Front Neurosci* **6**, 1–12 (2012).

37. Therriault, J. *et al.* Association of Phosphorylated Tau Biomarkers With Amyloid Positron Emission Tomography vs Tau Positron Emission Tomography. *JAMA Neurol* (2022) doi:10.1001/jamaneurol.2022.4485.

38. Karikari, T. K. *et al. Blood phosphorylated tau 181 as a biomarker for Alzheimer's disease: a diagnostic performance and prediction modelling study using data from four prospective cohorts*. *Articles Lancet Neurol* vol. 19 www.thelancet.com/neurology (2020).

39. Ashton, N. J. *et al.* Plasma p-tau231: a new biomarker for incipient Alzheimer's disease pathology. *Acta Neuropathol* **141**, 709–724 (2021).

40. Triana-Baltzer, G. *et al.* Development and validation of a high-sensitivity assay for measuring p217+tau in plasma. *Alzheimer's and Dementia: Diagnosis, Assessment and Disease Monitoring* **13**, (2021).

41. Benedet, A. L. *et al.* Differences between Plasma and Cerebrospinal Fluid Glial Fibrillary Acidic Protein Levels across the Alzheimer Disease Continuum. *JAMA Neurol* **78**, 1471–1483 (2021).

42. Ashton, N. J. *et al.* Plasma p-tau231: a new biomarker for incipient Alzheimer's disease pathology. *Acta Neuropathol* **141**, 709–724 (2021).

43. Tissot, C. *et al.* Plasma pTau181 predicts cortical brain atrophy in aging and Alzheimer's disease. *Alzheimers Res Ther* **13**, (2021).

44. Adewale, Q., Khan, A. F., Carbonell, F. & Iturria-Medina, Y. Integrated transcriptomic and neuroimaging brain model decodes biological mechanisms in aging and Alzheimer's disease. *Elife* **10**, (2021).

45. Khan, A. F. *et al.* Personalized brain models identify neurotransmitter receptor changes in Alzheimer's disease. *Brain* **145**, 1785–1804 (2022).

46. Braak, H., Braak, E. & Braak, E. *Staging of Alzheimer's Disease-Related Neurofibrillary Changes*. *Neurobiology of Aging* vol. 16 (1995).

47. Celone, K. A. *et al.* Alterations in memory networks in mild cognitive impairment and Alzheimer's disease: An independent component analysis. *Journal of Neuroscience* **26**, 10222–10231 (2006).

48. Ashton, N. J. *et al.* Differential roles of Aβ42/40, p-tau231 and p-tau217 for Alzheimer's trial selection and disease monitoring. *Nat Med* (2022) doi:10.1038/s41591-022-02074-w.

49. Milà-Alomà, M. *et al.* Plasma p-tau231 and p-tau217 as state markers of amyloid-β pathology in preclinical Alzheimer's disease. *Nat Med* **28**, 1797–1801 (2022).

50. Nutma, E. *et al.* Translocator protein is a marker of activated microglia in rodent models but not human neurodegenerative diseases. doi:10.1101/2022.05.11.491453.

51. Tan Toi, P. *et al. In vivo direct imaging of neuronal activity at high temporospatial resolution*. https://www.science.org.

52. Mederos, S. & Perea, G. GABAergic-astrocyte signaling: A refinement of inhibitory brain networks. *GLIA* vol. 67 1842–1851 Preprint at https://doi.org/10.1002/glia.23644 (2019).

53. Deco, G. *et al. Dynamical consequences of regional heterogeneity in the brain's transcriptional landscape*. *Sci. Adv* vol. 7 https://www.science.org (2021).

54. Sotero, R. C. & Trujillo-Barreto, N. J. Biophysical model for integrating neuronal activity, EEG, fMRI and metabolism. *Neuroimage* **39**, 290–309 (2008).

55. Tissot, C. *et al.* The association of age-related and off-target retention with longitudinal quantification of [18 F]MK6240 tau-PET in target regions. doi:10.1101/2022.05.24.22275386.

56. Vogel, J. W. *et al.* Spread of pathological tau proteins through communicating neurons in human Alzheimer's disease. *Nat Commun* **11**, 2612 (2020).

57. Young, P. N. E. *et al.* Imaging biomarkers in neurodegeneration: Current and future practices. *Alzheimer's Research and Therapy* vol. 12 Preprint at https://doi.org/10.1186/s13195-020-00612-7 (2020).

58. Evans, A. C., Kamber, M., Collins, D. L. & MacDonald, D. An MRI-Based Probabilistic Atlas of Neuroanatomy. in *Magnetic Resonance Scanning and Epilepsy* 263–274 (Springer US, 1994). doi:10.1007/978-1-4615-2546-2_48.

59. Iturria-Medina, Y. *et al.* Characterizing brain anatomical connections using diffusion weighted MRI and graph theory. *Neuroimage* **36**, 645–660 (2007).

60. Tournier, J. D. *et al.* Resolving crossing fibres using constrained spherical deconvolution: Validation using diffusion-weighted imaging phantom data. *Neuroimage* **42**, 617–625 (2008).

61. Sanchez-Rodriguez, L. M., Iturria-Medina, Y., Mouches, P. & Sotero, R. C. Detecting brain network communities: Considering the role of information flow and its different temporal scales. *Neuroimage* **225**, 117431 (2021).

62. Pascoal, T. A. *et al.* 18F-MK-6240 PET for early and late detection of neurofibrillary tangles. *Brain* **143**, 2818–2830 (2020).

63. Therriault, J. *et al.* Biomarker modeling of Alzheimer's disease using PET-based Braak staging. *Nat Aging* **2**, 526–535 (2022).

64. Wilson, H. R. & Cowan, J. D. Excitatory and inhibitory interactions in localized populations of model neurons. *Biophys J* **12**, 1–24 (1972).

65. Daffertshofer, A. & van Wijk, B. C. M. On the Influence of Amplitude on the Connectivity between Phases. *Front Neuroinform* **5**, 6 (2011).

66. Abeysuriya, R. G. *et al.* A biophysical model of dynamic balancing of excitation and inhibition in fast oscillatory large-scale networks. (2018).

67. Meijer, H. G. E. *et al.* Modeling focal epileptic activity in the Wilson-cowan model with depolarization block. *J Math Neurosci* **5**, 7 (2015).

68. Gjorgjieva, J., Evers, J. F. & Eglen, S. J. Homeostatic activity-dependent tuning of recurrent networks for robust propagation of activity. *Journal of Neuroscience* **36**, 3722–3734 (2016).

69. Jansen, B. H. & Rit, V. G. Electroencephalogram and visual evoked potential generation in a mathematical model of coupled cortical columns. *Biol Cybern* **73**, 357–366 (1995).

70. Deco, G., Jirsa, V., Mcintosh, A. R., Sporns, O. & Ko, R. Key role of coupling , delay , and noise in resting brain fluctuations. **106**, (2009).

71. Logothetis, N. K., Pauls, J., Augath, M., Trinath, T. & Oeltermann, A. Neurophysiological investigation of the basis of the fMRI signal. (2001).

72. Valdes-Sosa, P. A. *et al.* Model driven EEG/fMRI fusion of brain oscillations. *Hum Brain Mapp* **30**, 2701–2721 (2009).

73. Sotero, R. C. & Trujillo-Barreto, N. J. Modelling the role of excitatory and inhibitory neuronal activity in the generation of the BOLD signal. *Neuroimage* **35**, 149–165 (2007).

74. Sotero, R. C., Trujillo-Barreto, N. J., Jiménez, J. C., Carbonell, F. & Rodríguez-Rojas, R. Identification and comparison of stochastic metabolic/hemodynamic models (sMHM) for the generation of the BOLD signal. *J Comput Neurosci* **26**, 251–69 (2009).

75. Friston, K. J., Mechelli, A., Turner, R. & Price, C. J. Nonlinear responses in fMRI: The balloon model, Volterra kernels, and other hemodynamics. *Neuroimage* **12**, 466–477 (2000).

76. Buxton, R. B., Wong, E. C. & Frank, L. R. Dynamics of blood flow and oxygenation changes during brain activation: The balloon model. *Magn Reson Med* **39**, 855–864 (1998).

77. Obata, T. *et al.* Discrepancies between BOLD and flow dynamics in primary and supplementary motor areas : application of the balloon model to the interpretation of BOLD transients. **21**, 144–153 (2004).

78. Simon, A. B. & Buxton, R. B. Understanding the dynamic relationship between cerebral blood flow and the BOLD signal: Implications for quantitative functional MRI. *Neuroimage* **116**, 158–167 (2015).

79. Archila-Meléndez, M. E., Sorg, C. & Preibisch, C. Modeling the impact of neurovascular coupling impairments on BOLD-based functional connectivity at rest. *Neuroimage* **218**, (2020).

Acknowledgments

We thank Cristopher J. Steele and Abbas Sadikot for their comments on the results and limitations. LSR was partially supported by funding from the Fonds de recherche du Québec – Santé and the Healthy Brains for Healthy Lives (HBHL) initiative. This project was undertaken thanks in part to the following funding awarded to YIM: the Canada Research Chair tier-2, the CIHR Project Grant 2020, and the Weston Family Foundation's AD Rapid Response 2018 and Transformational Research in AD 2020. In addition, we used the computational infrastructure of the McConnell Brain Imaging Center at the Montreal Neurological Institute, supported in part by the *Brain Canada Foundation*, through the *Canada Brain Research Fund*, with the financial support of *Health Canada* and sponsors. PRN, GB, JT and JF are supported by the Canadian Institutes of Health Research (CIHR) [MOP-11-51-31; RFN 152985, 159815, 162303], Canadian Consortium of Neurodegeneration and Aging (CCNA; MOP-11-51-31 -team 1), Weston Brain Institute, the Alzheimer's Association [NIRG-12-92090, NIRP-12-259245], Brain Canada Foundation (CFI Project 34874; 33397), the Fonds de Recherche du Québec – Santé (FRQS; Chercheur Boursier, 2020-VICO-279314) and the Colin J. Adair Charitable Foundation. HZ is a Wallenberg Scholar supported by grants from the Swedish Research Council (#2022-01018), the European Union's Horizon Europe research and innovation programme under grant agreement No 101053962, Swedish State Support for Clinical Research (#ALFGBG-71320), the Alzheimer Drug Discovery Foundation (ADDF), USA (#201809-2016862), the AD Strategic Fund and the Alzheimer's Association (#ADSF-21-831376-C, #ADSF-21-831381-C, and #ADSF-21-831377-C), the Bluefield Project, the Olav Thon Foundation, the Erling-Persson Family Foundation, Stiftelsen för Gamla Tjänarinnor, Hjärnfonden, Sweden (#FO2022-0270), the European Union's Horizon 2020 research and innovation programme under the Marie Skłodowska-Curie grant

agreement No 860197 (MIRIADE), the European Union Joint Programme – Neurodegenerative Disease Research (JPND2021-00694), and the UK Dementia Research Institute at UCL (UKDRI-1003). KB is supported by the Swedish Research Council (#2017-00915 and #2022-00732), the Alzheimer Drug Discovery Foundation (ADDF), USA (#RDAPB-201809-2016615), the Swedish Alzheimer Foundation (#AF-930351, #AF-939721 and #AF-968270), Hjärnfonden, Sweden (#FO2017-0243 and #ALZ2022-0006), the Swedish state under the agreement between the Swedish government and the County Councils, the ALF-agreement (#ALFGBG-715986 and #ALFGBG-965240), the European Union Joint Program for Neurodegenerative Disorders (JPND2019-466-236), the National Institute of Health (NIH), USA, (grant #1R01AG068398-01), the Alzheimer's Association 2021 Zenith Award (ZEN-21-848495), and the Alzheimer's Association 2022-2025 Grant (SG-23-1038904 QC). TKK was funded by the Swedish Research Council (Vetenskapsrådet #2021-03244), the Alzheimer's Association Research Fellowship (#AARF-21-850325), the Swedish Alzheimer Foundation (Alzheimerfonden), the Aina (Ann) Wallströms and Mary-Ann Sjöbloms stiftelsen, and the Emil och Wera Cornells stiftelsen.

Author contributions

LSR and YIM conceived the theoretical formalism. PRN, TK, NA, AB, HZ, KB, GT, HK collected the data. GB and LSR processed the data. LSR implemented the algorithm and performed the computations. YIM, FC, GB, JT and JFA contributed to the analyses. LSR wrote the manuscript draft. YIM supervised the project. All authors discussed the results and contributed to the final manuscript.

Competing interests

HZ has served at scientific advisory boards and/or as a consultant for Abbvie, Acumen, Alector, Alzinova, ALZPath, Annexon, Apellis, Artery Therapeutics, AZTherapies, CogRx, Denali, Eisai, Nervgen, Novo Nordisk, Optoceutics, Passage Bio, Pinteon Therapeutics, Prothena, Red Abbey Labs, reMYND, Roche, Samumed, Siemens Healthineers, Triplet Therapeutics, and Wave, has given lectures in symposia sponsored by Cellectricon, Fujirebio, Alzecure, Biogen, and Roche, and is a co-founder of Brain Biomarker Solutions in Gothenburg AB (BBS), which is a part of the GU Ventures Incubator Program (outside submitted work). KB has served as a consultant, at advisory boards, or at data monitoring committees for Acumen, ALZPath, BioArctic, Biogen, Eisai, Julius Clinical, Lilly, Novartis, Ono Pharma, Prothena, Roche Diagnostics, and Siemens Healthineers, and is a co-founder of Brain Biomarker Solutions in Gothenburg AB (BBS), which is a part of the GU Ventures Incubator Program, outside the work presented in this paper. The other authors declare no competing interests.

Supplementary Information

Revealing the combined roles of Aβ and tau in Alzheimer's disease via a pathophysiological activity decoder

Sanchez-Rodriguez et al.

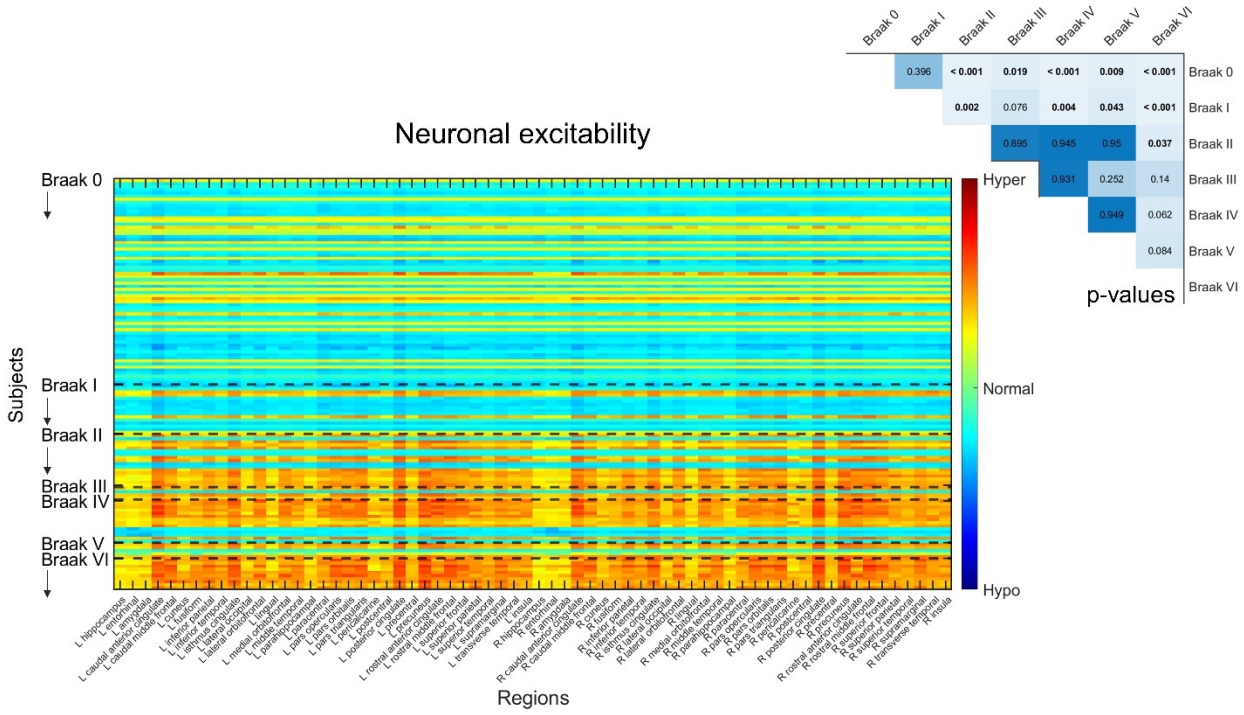

Supplementary Fig. 1. Neuronal excitabilities under the influence of *Aβ, tau and Aβ·tau*. Participants were grouped according to Braak stages. Inferred neuronal excitability values for the brain regions of interest ("y"-axis) and all subjects ("x"-axis). Within a group, subjects appear according to their existing ordering in the anonymized database. Warm colors represent hyperexcitability of the region in the subject's brain and cool colors denote hypoexcitable states. Results of ANCOVA post-hoc t-tests for the above-mentioned groups, with the average intra-brain excitability values as response variable and age and sex as covariates appear in the upper right corner. P-values in bold fonts represent differences at a 5% significance level or lower. This figure is analogous to Fig. 3

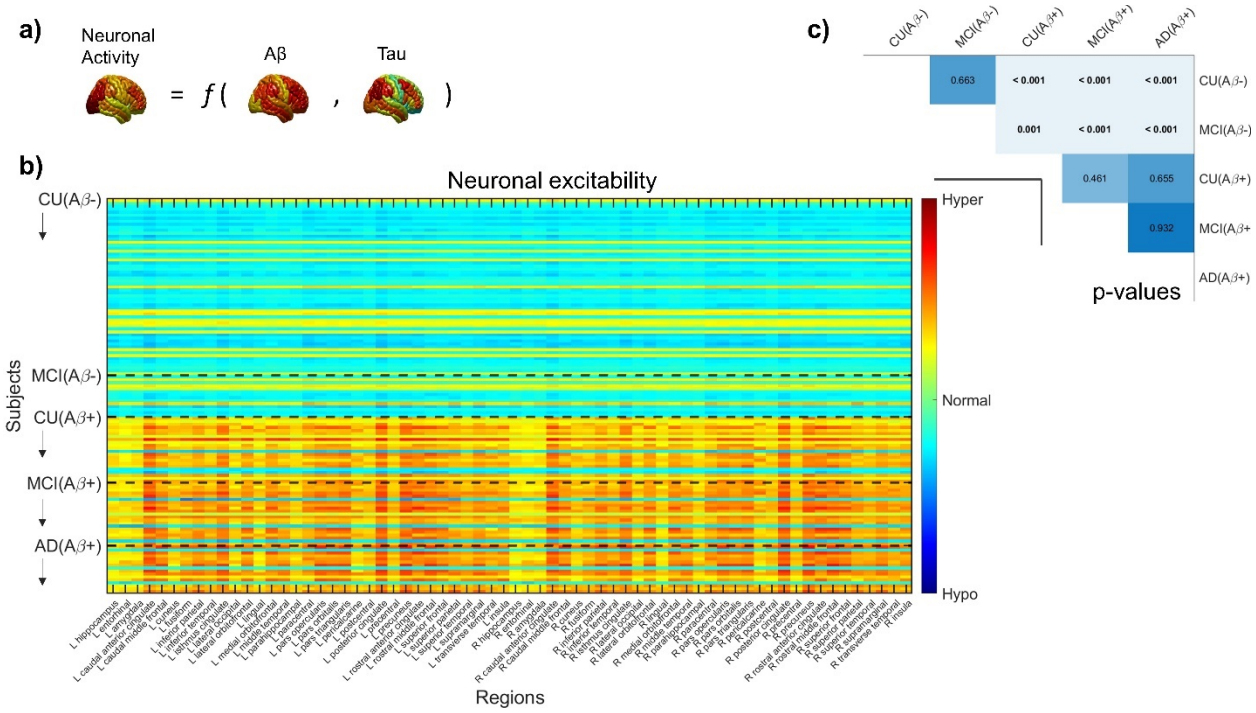

Supplementary Fig. 2. Neuronal excitabilities under the influence of *Aβ and tau* (participants grouped according to Aβ-positivity). **a**) Schematic representation of the influence model. **b**) Inferred neuronal excitability values for the brain regions of interest ("y"-axis) and all subjects ("x"-axis). Within a group, subjects appear according to their existing ordering in the anonymized database. Warm colors represent hyperexcitability of the region in the subject's brain and cool colors denote hypoexcitable states. **c**) Results of ANCOVA post-hoc t-tests for the above-mentioned groups, with the average intra-brain excitability values as response variable and age and sex as covariates. P-values in bold fonts represent differences at a 5% significance level or lower.

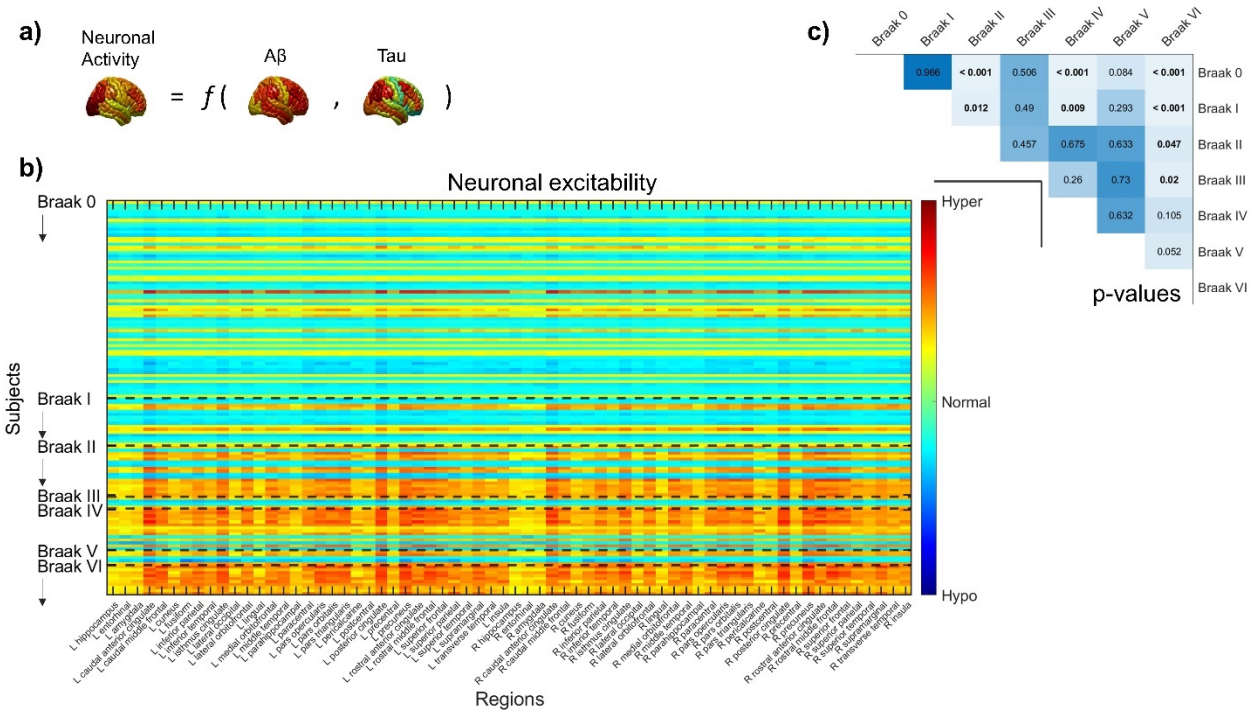

Supplementary Fig. 3. Neuronal excitabilities under the influence of *Aβ and tau* (participants grouped according to Braak stages). a) Schematic representation of the influence model. **b**) Inferred neuronal excitability values for the brain regions of interest ("y"-axis) and all subjects ("x"-axis). Within a group, subjects appear according to their existing ordering in the anonymized database. Warm colors represent hyperexcitability of the region in the subject's brain and cool colors denote hypoexcitable states. **c**) Results of ANCOVA post-hoc t-tests for the above-mentioned groups, with the average intra-brain excitability values as response variable and age and sex as covariates. P-values in bold fonts represent differences at a 5% significance level or lower.

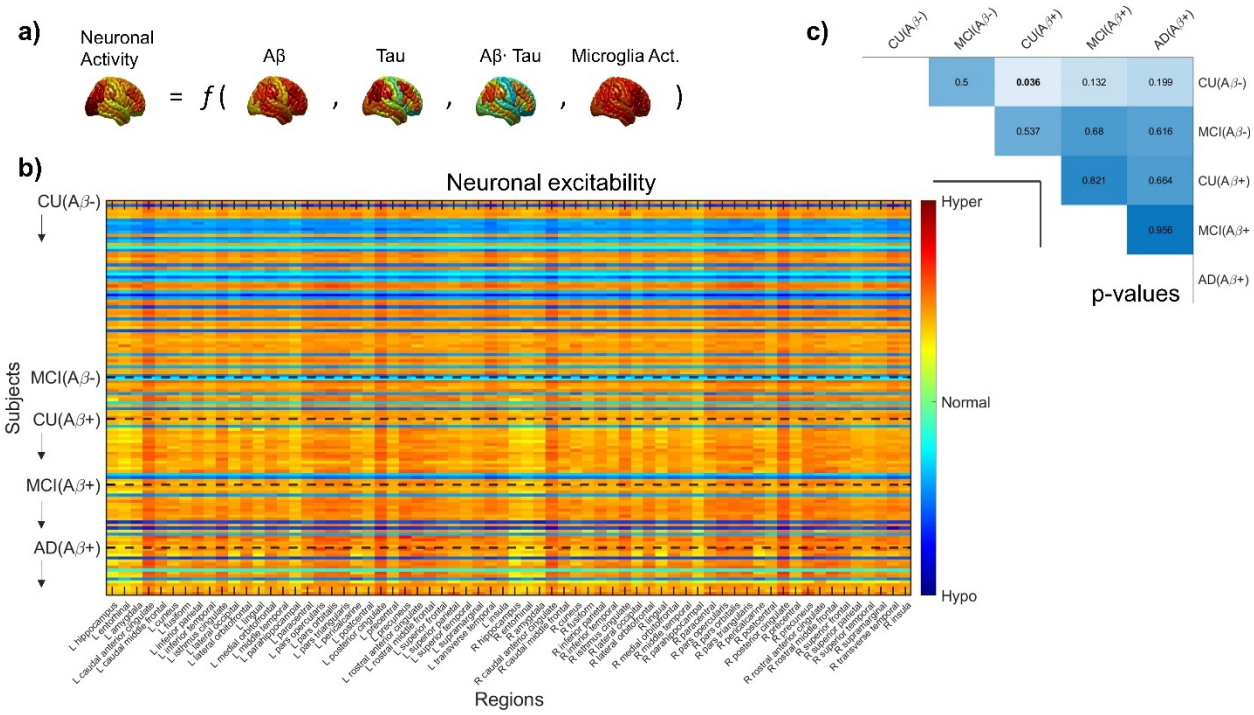

Supplementary Fig. 4. Neuronal excitabilities under the influence of *Aβ, tau, Aβ·tau and microglial activation* (participants grouped according to Aβ-positivity). **a**) Schematic representation of the influence model. **b**) Inferred neuronal excitability values for the brain regions of interest ("y"-axis) and all subjects ("x"-axis). Within a group, subjects appear according to their existing ordering in the anonymized database. Warm colors represent hyperexcitability of the region in the subject's brain and cool colors denote hypoexcitable states. **c**) Results of ANCOVA post-hoc t-tests for the above-mentioned groups, with the average intra-brain excitability values as response variable and age and sex as covariates. No significant differences between groups were observed.

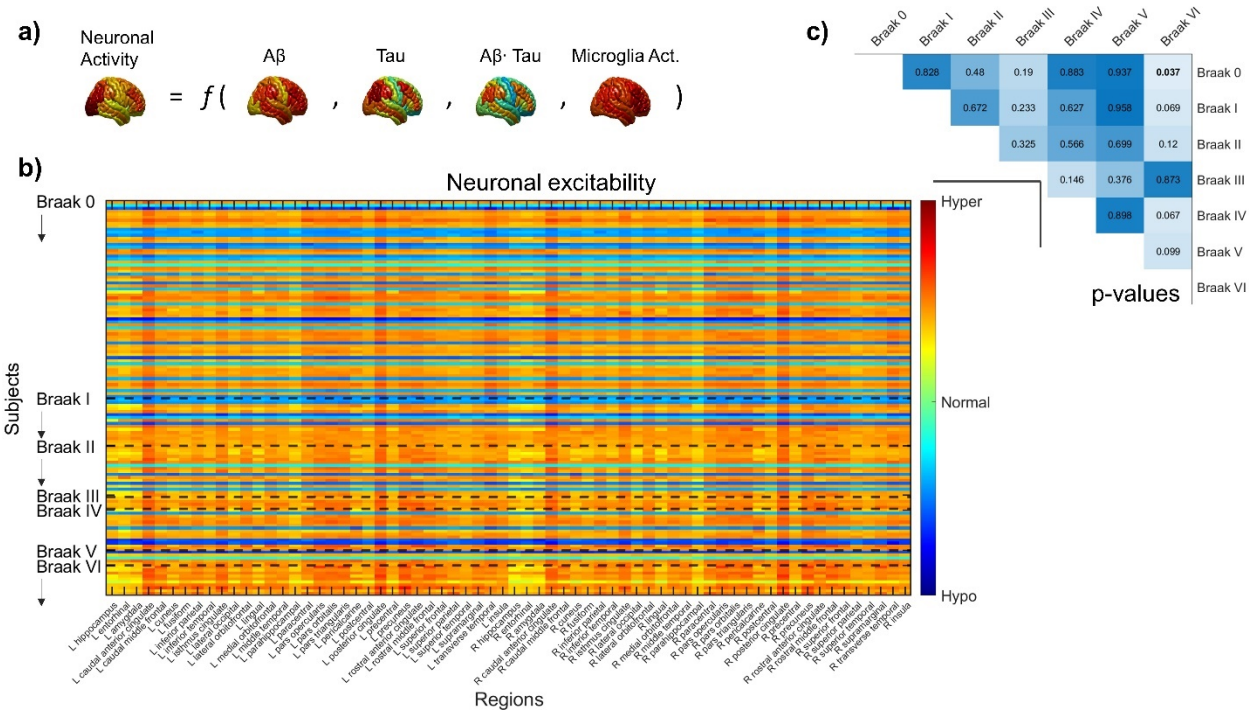

Supplementary Fig. 5. Neuronal excitabilities under the influence of *Aβ, tau, Aβ·tau and microglial activation* (participants grouped according to Braak stages). a) Schematic representation of the influence model. **b**) Inferred neuronal excitability values for the brain regions of interest ("y"-axis) and all subjects ("x"-axis). Within a group, subjects appear according to their existing ordering in the anonymized database. Warm colors represent hyperexcitability of the region in the subject's brain and cool colors denote hypoexcitable states. **c**) Results of ANCOVA post-hoc t-tests for the above-mentioned groups, with the average intra-brain excitability values as response variable and age and sex as covariates. P-values in bold fonts represent differences at a 5% significance level or lower.

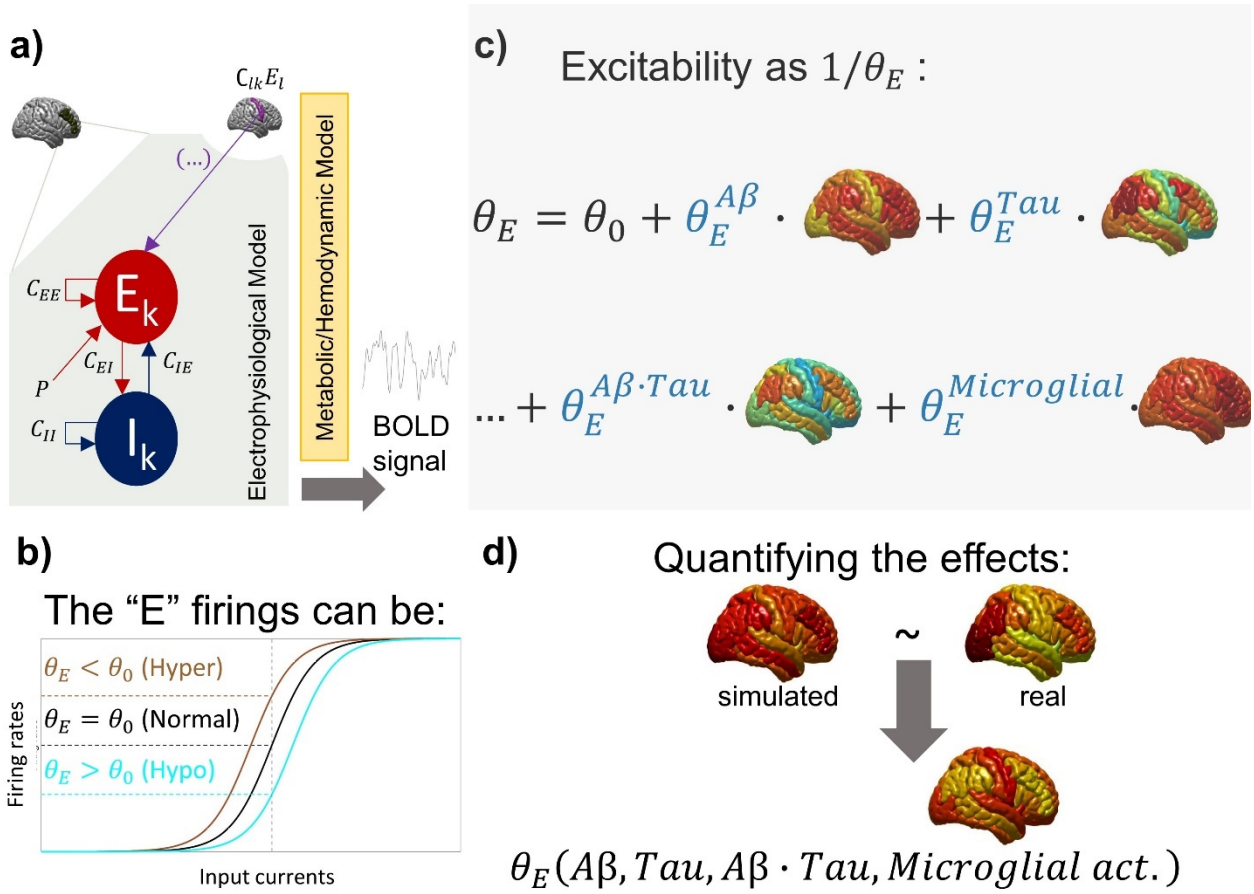

Supplementary Fig. 6. Overview of integrating pathophysiological information into the computational brain activity decoder for Alzheimer's. a) Each brain region, k, is modeled as coupled excitatory and inhibitory populations. For example, C_{EI} represents the strength of the excitatory connection with the inhibitory neural mass. Additionally, the excitatory population receives an unspecified local stimulus that accounts for unmodeled interactions, P, and excitatory inputs from other regions via a connectivity matrix obtained from diffusion MRI (C_{lk}). The excitatory and inhibitory inputs feed a metabolic/hemodynamic model that simulates the resting-state BOLD signal (fMRI) for the given region. **b**) In the study, the excitatory firing rates are obtained by using sigmoid functions with varying firing thresholds. A low sigmoidal threshold value means high firing rates ("hyperexcitable state") at a given input current, while the opposite is termed "hypoexcitability", as compared to baseline firing conditions. **c**) The influence of pathophysiological factors on neuronal activity is modeled as linear changes on a region's firing threshold due to the competition/contribution of the regional pathological loads. In Alzheimer's disease, we assume that the threshold can be, in general, affected by Aβ plaques, tau tangles, the interaction of Aβ and tau (modeled as the regional multiplication of the Aβ and tau SUVRs), and microglial activation. Thus, the anatomical representations in the figure gather PET SUVRs corresponding to these factors in 66 regions of interest. The proportionality constants (θ_E^{Ab}, θ_E^{Tau}, $\theta_E^{Ab \cdot Tau}$, $\theta_E^{Microglial\ act.}$) characterize the subject-specific global influence of the pathologies. **d**) We infer these pathological influences by minimizing the similarity between the observed neuronal activity biomarkers (i.e., the fractional amplitude of low-

frequency fluctuations in the regional BOLD signals) and the analogous indicators in the simulated signals, for each of the participants. With the obtained global influences, we reconstruct hidden excitability maps based on the pathology-dependent neuronal firing thresholds.

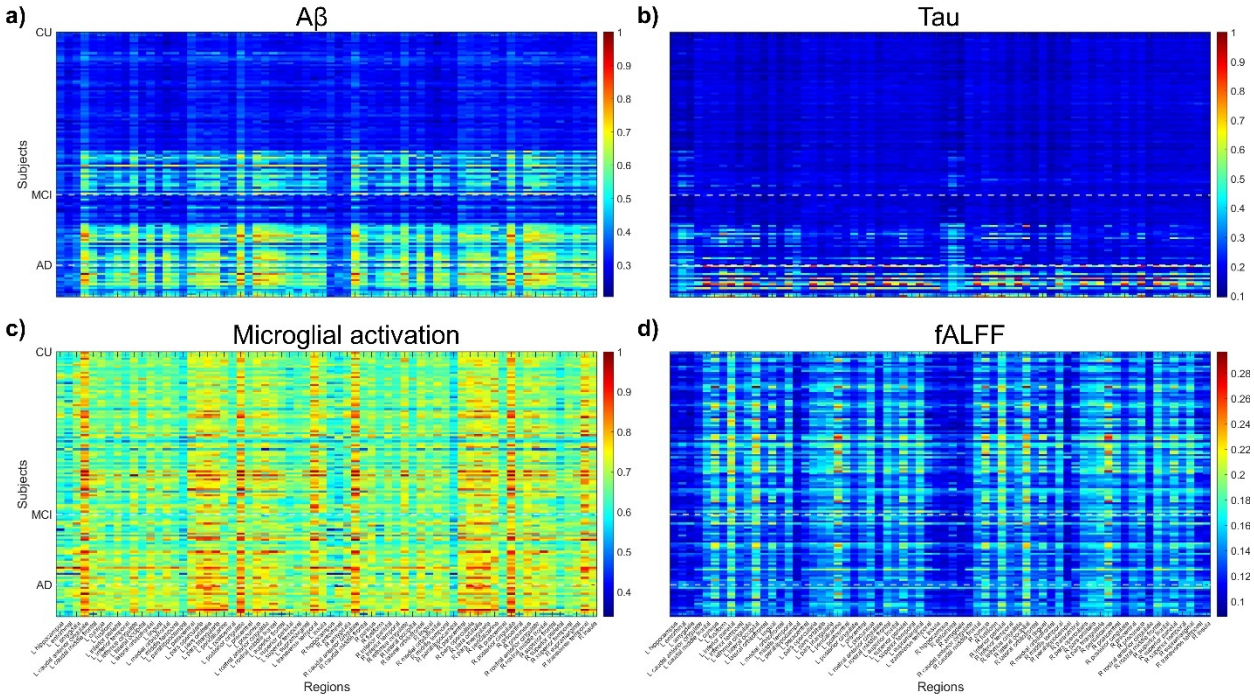

Supplementary Fig. 7. Distributions of the processed data that was utilized in the study. a) Aβ PET SUVRs **b**) Tau PET SUVRs **c**) Microglial activation PET SUVRs **d**) Fractional amplitudes of low-frequency fluctuations (fALFF) from fMRI. Subjects are organized by clinical groups (CU, MCI, AD) and appear in the same order as in Fig. 3 within a given clinical group. The SUVRs were normalized to the [0,1] interval by dividing by the absolute maximum value corresponding to each imaging modality.

Supplementary Table 1. Demographics of the samples

	CU	MCI	p	AD	p
Number of individuals (N)	81	35	-	16	-
Age (yrs), mean (s.d.)	71.15 (7.73)	72.17 (7.84)	0.517	69.45 (9.10)	0.438
Female, N (%)	63 (77.8)	17 (48.6)	0.004	8 (50.0)	0.031
Education (yrs), mean (s.d.)	15.26 (3.54)	15.63 (3.01)	0.591	14.31 (3.38)	0.327
APOE ε4 carriers, N (%)	24 (29.6)	17 (48.6)	0.059	7 (43.8)	0.379
MMSE, mean (s.d.)	29.28 (0.97)	28.40 (1.54)	< 0.001	20.25 (7.20)	< 0.001
Aβ+, N (%)	20 (24.7)	23 (65.7)	0.006	16 (100.0)	< 0.001

The reported p-values are for comparisons to cognitively unimpaired (CU) subjects. P-values for age, education and MMSE indicate values assessed with two-sided independent-samples t-tests. For the resting variables (sex, *APOE* ε4 status and Aβ+), Fischer exact test were performed. CU cognitively unimpaired; MCI mild cognitive impairment; AD Alzheimer's disease; *APOE* ε4, apolipoprotein epsilon 4; MMSE, Mini-Mental State examination; PET, positron emission tomography.

Supplementary Table 2. Results of statistical tests

Quantity	Test	Group 1	Group 2	F-Statistic	dfe	p
Ratio of power in theta band^	ANCOVA post-hoc t-tests	CU(Aβ-)	CU(Aβ+)	40.77	77	< 0.001
		CU(Aβ-)	MCI(Aβ+)	53.62	76	< 0.001
		CU(Aβ-)	AD(Aβ+)	41.00	71	< 0.001
		MCI(Aβ-)	CU(Aβ+)	15.54	32	0.018
		MCI(Aβ-)	MCI(Aβ+)	15.54	31	< 0.001
		MCI(Aβ-)	AD(Aβ+)	13.89	26	< 0.001
		Braak 0	Braak II	14.46	79	< 0.001
		Braak 0	Braak IV	11.87	76	< 0.001
		Braak 0	Braak V	6.00	67	0.016
		Braak 0	Braak VI	30.52	72	< 0.001
		Braak I	Braak II	11.63	29	0.002
		Braak I	Braak IV	9.83	26	0.004
		Braak I	Braak V	5.41	17	0.032
		Braak I	Braak VI	25.17	22	< 0.001
Ratio of power in alpha1 band^	ANCOVA post-hoc t-tests	CU(Aβ-)	CU(Aβ+)	18.72	77	< 0.001
		CU(Aβ-)	MCI(Aβ+)	25.93	76	< 0.001
		CU(Aβ-)	AD(Aβ+)	19.06	71	< 0.001
		MCI(Aβ-)	MCI(Aβ+)	10.58	31	0.003
		MCI(Aβ-)	AD(Aβ+)	9.81	26	0.004
		Braak 0	Braak II	5.85	79	0.018
		Braak 0	Braak IV	5.12	76	0.026
		Braak 0	Braak V	4.13	67	0.046
		Braak 0	Braak VI	11.70	72	0.001
		Braak I	Braak II	8.65	29	0.006
		Braak I	Braak IV	8.12	26	0.008
		Braak I	Braak V	5.62	17	0.030
		Braak I	Braak VI	12.92	22	0.002
Mean excitatory activity^	ANCOVA post-hoc t-tests	CU(Aβ-)	CU(Aβ+)	52.44	77	< 0.001
		CU(Aβ-)	MCI(Aβ+)	62.28	76	< 0.001
		CU(Aβ-)	AD(Aβ+)	49.87	71	< 0.001
		MCI(Aβ-)	CU(Aβ+)	9.38	32	0.004
		MCI(Aβ-)	MCI(Aβ+)	22.07	31	< 0.001
		MCI(Aβ-)	AD(Aβ+)	18.95	26	< 0.001
		Braak 0	Braak II	16.41	79	< 0.001
		Braak 0	Braak III	5.16	66	0.026
		Braak 0	Braak IV	13.08	76	< 0.001
		Braak 0	Braak V	6.78	67	0.011
		Braak 0	Braak VI	40.99	72	< 0.001
		Braak I	Braak II	11.56	29	0.002
		Braak I	Braak IV	9.79	26	0.004
		Braak I	Braak V	4.91	17	0.041
		Braak I	Braak VI	29.80	22	< 0.001
		Braak II	Braak VI	4.52	23	0.044

Average intra-brain excitability^	ANCOVA post-hoc t-tests	CU(Aβ-)	CU(Aβ+)	55.54	77	< 0.001
		CU(Aβ-)	MCI(Aβ+)	66.06	76	< 0.001
		CU(Aβ-)	AD(Aβ+)	54.19	71	< 0.001
		MCI(Aβ-)	CU(Aβ+)	9.96	32	0.003
		MCI(Aβ-)	MCI(Aβ+)	22.65	31	< 0.001
		MCI(Aβ-)	AD(Aβ+)	19.78	26	< 0.001
		Braak 0	Braak II	17.80	79	< 0.001
		Braak 0	Braak III	5.99	66	0.019
		Braak 0	Braak IV	14.67	76	< 0.001
		Braak 0	Braak V	7.58	67	0.009
		Braak 0	Braak VI	46.36	72	< 0.001
		Braak I	Braak II	9.46	29	0.002
		Braak I	Braak IV	8.66	26	0.004
		Braak I	Braak V	27.30	17	0.043
		Braak I	Braak VI	4.91	22	< 0.001
		Braak II	Braak VI	4.52	23	0.037
Plasma biomarkers	Spearman correlation	Mean excitability	p-tau181	NA	NA	0.003
		Mean excitability	p-tau231	NA	NA	0.003
		Mean excitability	p-tau217	NA	NA	< 0.001
		Mean excitability	GFAP	NA	NA	< 0.001
MMSE*	Linear regression model	NA	NA	4.43	123	< 0.001
MoCA*	Linear regression model	NA	NA	4.58	120	< 0.001

CU cognitively unimpaired; MCI mild cognitive impairment; AD Alzheimer's disease; ^ sex and age adjusted; * sex, age and education adjusted.

Supplementary Table 3. Multiple linear regression analysis investigating the pathological effects on neuronal activity as predictors of MMSE and MoCA scores in the *Aβ, tau, Aβ·tau, microglial activation* influence model

MMSE scores			
	β	95% CI of β	p
Intercept	27.136	[21.110 34.161]	< 0.001
$\theta^{A\beta}$	0.373	[-0.296 1.041]	0.272
θ^{Tau}	0.151	[-0.524 0.837]	0.659
$\boldsymbol{\theta^{A\beta\cdot Tau}}$	**1.530**	**[0.856 2.205]**	**< 0.001**
$\theta^{microglial\ act.}$	45	[-1.1402 0.249]	0.201
Sex	-0.960	[-2.348 0.429]	0.174
Age	0.009	[-0.080 0.099]	0.834
Education	0.029	[-0.163 0.221]	0.762
MoCA scores			
	β	95% CI of β	p
Intercept	22.145	[11.994 32.296]	< 0.001
$\boldsymbol{\theta^{A\beta}}$	**1.004**	**[0.081 1.927]**	**0.033**
θ^{Tau}	0.129	[-0.791 1.048]	0.782
$\boldsymbol{\theta^{A\beta\cdot Tau}}$	**1.966**	**[1.024 2.888]**	**< 0.001**
$\theta^{microglial\ act.}$	-0.609	[-1.565 0.347]	0.209
Sex	-1.624	[-3.570 0.322]	0.101
Age	0.058	[-0.073 0.189]	0.380
Education	-0.025	[-0.2920 0.2424]	0.855

The influences of Aβ plaques ($\theta_E^{A\beta}$), tau tangles (θ_E^{Tau}), the interaction of Aβ and tau ($\theta_E^{A\beta\cdot Tau}$) and microglial activation ($\theta_E^{microglial\ act.}$) on neuronal activity, sex, age and education were considered as predictors. Reported values are obtained coefficients (β), the 95% confidence intervals and the p-values for the t-statistic of the two-sided hypothesis tests. Significant terms (5% level) other than the intercepts are highlighted. MMSE: R^2=0.19, p < 0.001; MoCA: R^2=0.21, p < 0.001. MMSE, Mini-Mental State examination; MoCA, Montreal Cognitive Assessment.

Supplementary Table 4. Brain regions in the considered parcellation.

Hippocampus	Lateral Orbitofrontal^{B}	Posterior Cingulate
Entorhinal^{R}	Medial Orbitofrontal^{R}	Precentral
Amygdala	Lingual^{L}	Precuneus^{B}
Caudal Anterior Cingulate	Middle Temporal^{B}	Rostral Anterior Cingulate
Caudal Middle Frontal	Parahippocampal^{B}	Rostral Middle Frontal
Cuneus	Paracentral	Superior Frontal
Fusiform^{B}	Pars Opercularis^{R}	Superior Parietal
Inferior Parietal^{R}	Pars Orbitalis^{2}	Superior Temporal
Inferior Temporal^{B}	Pars Triangularis^{R}	Supramarginal
Isthmus Cingulate^{L}	Pericalcarine^{L}	Transverse Temporal
Lateral Occipital^{B}	Postcentral	Insula

Regions with a superscript next to the name have statistically different microglial activation PET SUVRs when comparing the CU and AD groups: ^{B} - bilaterally different, ^{L} - only the values of the left hemisphere region is different, ^{R} - only the values of the right hemisphere region is different.

Supplementary Table 5. Electrophysiological model parameters

Parameter	Definition	Value	Ref.
τ_I	Time-constant controlling the decay of inhibitory activity after stimulation	0.02 s	[1]
τ_E	Time-constant controlling the decay of excitatory activity after stimulation	0.01 s	[1]
C_{II}	Local inhibitory-inhibitory connection strength	1.2	[2–4]
C_{EI}	Local excitatory-inhibitory connection strength	6	[2–4]
C_{EE}	Local excitatory-excitatory connection strength	6.4	[2–4]
C_{IE}	Local inhibitory-excitatory connection strength	4.8	[2–4]
P	Average constant external input received by the excitatory population	0.65 (set to produce plausible simulated electrophysiological and BOLD signals)	[2–4]
a_I	Maximum slope of the inhibitory sigmoidal activation function	1	[1]
a_E	Maximum slope of the excitatory sigmoidal activation function	1	[1]
θ_I	Position of the inhibitory sigmoidal firing function' threshold for activation	4	[2–4]
θ_E	Position of the excitatory sigmoidal firing function' threshold for activation	Variable in [2.75,2.85] depending on the regional pathological loads 2.8 (in normal baseline conditions)	[1–5]
η	Global coupling strength scaling the anatomical connectivity matrix C_{lk}	2 (set to produce plausible simulated electrophysiological and BOLD signals)	[1–5]
N	Number of brain regions of interest	66	[6]

Supplementary Table 6. Metabolic/hemodynamic model parameters

Parameter	Definition	Value	Ref.
h_E	Efficacy of glucose consumption response to excitation	1	[7–10]
h_I	Efficacy of glucose consumption response to inhibition	1	[7–10]
$\varkappa_E$	Time-constant of the excitatory glucose consumption impulse response.	1 s	[7–10]
$\varkappa_I$	Time-constant of the inhibitory glucose consumption impulse response.	1 s	[7–10]
c	Steepness of the sigmoid function$x$	2.5	[7–10]
d	Position of the threshold of the sigmoid function x	1.6	[7–10]
γ	Baseline ratio of excitatory to inhibitory synaptic activity in the voxel	5	[7–10]
x_0	Fraction of glucose following the glycogenolitic pathway at rest	$\frac{1}{1+exp[c(d-1(t))]}$	[7–10]
μ	Efficacy of blood flow response to excitation	0.8	[7–10]
$\varkappa_f$	Time constant for CBF response	1.7	[7–10]
$\varkappa_0$	Transit time through the balloon	1	[7–10]
ζ	Coefficient of the steady state flow-volume relationship	0.4	[7–10]
V_0	Baseline blood volume	0.03	[7–10]
Υ_0	frequency offset of a fully deoxygenated blood vessel at 3 T	80.6 s^{-1} (at 3 T)	[11–13]
r_0	Slope defining the dependence of the R2*relaxation rate on blood oxygenation	178 s^{-1} (at 3 T)	[11–13]
E_0	Baseline oxygen extraction fraction	0.4	[11–13]
ε	Intrinsic ratio of blood to tissue signals at rest	0.24	[11–13]
TE	Echo time	32.0 ms	https://triad.tnl-mcgill.com/

References

1. Abeysuriya, R. G. *et al.* A biophysical model of dynamic balancing of excitation and inhibition in fast oscillatory large-scale networks. (2018).

2. Gjorgjieva, J., Evers, J. F. & Eglen, S. J. Homeostatic activity-dependent tuning of recurrent networks for robust propagation of activity. *Journal of Neuroscience* **36**, 3722–3734 (2016).

3. Meijer, H. G. E. *et al.* Modeling focal epileptic activity in the Wilson-cowan model with depolarization block. *J Math Neurosci* **5**, 7 (2015).

4. Wilson, H. R. & Cowan, J. D. Excitatory and inhibitory interactions in localized populations of model neurons. *Biophys J* **12**, 1–24 (1972).

5. Daffertshofer, A. & van Wijk, B. C. M. On the Influence of Amplitude on the Connectivity between Phases. *Front Neuroinform* **5**, 6 (2011).

6. Klein, A. & Tourville, J. 101 Labeled Brain Images and a Consistent Human Cortical Labeling Protocol. *Front Neurosci* **6**, 1–12 (2012).

7. Sotero, R. C. & Trujillo-Barreto, N. J. Modelling the role of excitatory and inhibitory neuronal activity in the generation of the BOLD signal. *Neuroimage* **35**, 149–165 (2007).

8. Sotero, R. C. & Trujillo-Barreto, N. J. Biophysical model for integrating neuronal activity, EEG, fMRI and metabolism. *Neuroimage* **39**, 290–309 (2008).

9. Sotero, R. C., Trujillo-Barreto, N. J., Jiménez, J. C., Carbonell, F. & Rodríguez-Rojas, R. Identification and comparison of stochastic metabolic/hemodynamic models (sMHM) for the generation of the BOLD signal. *J Comput Neurosci* **26**, 251–69 (2009).

10. Valdes-Sosa, P. A. *et al.* Model driven EEG/fMRI fusion of brain oscillations. *Hum Brain Mapp* **30**, 2701–2721 (2009).

11. Obata, T. *et al.* Discrepancies between BOLD and flow dynamics in primary and supplementary motor areas : application of the balloon model to the interpretation of BOLD transients. **21**, 144–153 (2004).

12. Simon, A. B. & Buxton, R. B. Understanding the dynamic relationship between cerebral blood flow and the BOLD signal: Implications for quantitative functional MRI. *Neuroimage* **116**, 158–167 (2015).

13. Archila-Meléndez, M. E., Sorg, C. & Preibisch, C. Modeling the impact of neurovascular coupling impairments on BOLD-based functional connectivity at rest. *Neuroimage* **218**, (2020).